Experiments in Fluids (2026) 67:32
https://doi.org/10.1007/s00348-026-04185-3

RESEARCH ARTICLE

Characterizing floating particle clustering in free surface turbulence using LED-based PIV

Abhirath Anand[1] · **Christian Poelma**[1] · **Angeliki Laskari**[1]

Received: 26 June 2025 / Revised: 26 January 2026 / Accepted: 27 January 2026

Abstract

Dispersed two-phase flows at air–water interfaces are ubiquitous in environmentally relevant flows such as in the dispersion of floating microplastics or transport processes across the air–sea interface. In the current study, we propose a method to study such flows through the study of a relatively flat turbulent free surface laden with spherical floating particles ("floaters"). The free surface is perturbed by a relatively low-mean nearly homogeneous subsurface turbulent flow that is produced in a turbulence box actuated by a 10×10 synthetic jet array. The free surface flow field is characterized using planar particle image velocimetry (PIV) simultaneously with Lagrangian tracking of floaters allowing insight into the floater dynamics and the surface flow coupling. This is enabled by a relatively simple setup of LED panels and a single camera. Distinction between the continuous (flow tracers) and the dispersed (floaters) phase is carried out by exploiting their size disparity and number density. The proposed method is employed to characterize the single-phase flow field and the clustering statistics of floaters for different turbulence levels, the latter achieved by varying the distance of the free surface from the jet array. Specifically, we study the effect of different turbulence levels on the floater clustering behavior. We observe that the time required for floaters to reach a clustered quasi-steady state decreases with increasing vorticity and surface divergence amplitude. In addition, the growth rate of the mean cluster size is observed to increase with increasing vorticity and surface divergence amplitude, with its temporal evolution exhibiting two distinct phases: an agglomeration phase and an equilibrium phase. In contrast, in the absence of a subsurface flow, floaters are observed to cluster at a relatively slower rate characterized by a prolonged agglomeration phase. Finally, to highlight the potential of this technique in studying floater-laden turbulent free surfaces, preliminary results of flow–floater interactions are discussed.

1 Introduction

Transport along the free surface of a turbulent body of water is ubiquitous in both natural and industrial settings. Notable examples in nature include the transport of floating microplastics (Sutherland et al. 2023), oil slicks (Chen et al. 2016), and algal blooms (Abraham 1998), while in industrial processes, surface transport plays a key role in techniques such as flotation. Even when wave transport is negligible and the free surface remains relatively flat, surface transport is influenced by a multitude of surface features such as upwellings, downwellings, dimples, scars that are typical imprints of the bulk turbulent flow on the free surface; an extensive taxonomy and review of these surface features can be found in Brocchini and Peregrine (2001) and Muraro et al. (2021). While considerable attention has been given to the influence of the free surface on the subsurface turbulence and to the flow along the free surface, the latter receiving increased attention in recent literature, the behavior of floating particles on a turbulent free surface remains largely unexplored. In the current study, we present an experimental method to measure the flow *on* a relatively flat free surface below a nearly homogeneous turbulent subsurface flow while simultaneously tracking floating particles.

Knowledge background on air–water interface transport is remarkably vast and covers a wide range of scales. Here, we will primarily focus on insights from controlled laboratory and scale-resolving numerical studies on the topics of subsurface turbulence and floating particle transport. Such studies are by necessity small scale when compared to the majority of investigations in oceanic processes and transport of marine pollutants, which often employ *in situ* measurements, remote sensing, or large-scale simulations involving

✉ Abhirath Anand
A.Anand-1@tudelft.nl

[1] Process & Energy, Delft University of Technology, 2628 CB Delft, The Netherlands

Published online: 14 February 2026

some level of empiricism or modeling or both (Chamecki et al. 2019; van Sebille et al. 2020). In contrast, both experimental and numerical studies on subsurface turbulence and floating particle dynamics most commonly target the free surface in advection dominated open-channel flows, or in turbulence boxes where mean flow effects are usually minimal: Turbulence generation and development, its modulation due to the presence of the free surface, and, in turn, its effect on free surface deformation and floating particle clustering behavior are the main points of focus. In what follows, we will briefly discuss the main insights and open questions from these lines of research and make connections to the present study where relevant.

In the context of turbulence generation and characteristics, turbulence boxes allow turbulence to be studied in isolation from advection (i.e., in the absence of mean flows), particularly advantageous in investigating scalar transport and mixing. However, generating turbulence with a zero-mean flow is notoriously difficult and depends on the type of actuation; often, a trade-off must be made between the strength of the mean flow and the degree of isotropy, homogeneity, and spatial extent of the generated turbulence. Using two counter-rotating disks in a cylindrical container, Douady et al. (1991), and later Voth et al. (1998), generated a high–Reynolds number turbulent flow with negligible mean shear, albeit anisotropic at large scales and homogeneous only within a small central region (Voth et al. 2002). A combination of high isotropy and homogeneity at high Reynolds number has been achieved through systems utilizing multiple loudspeakers (Hwang and Eaton 2004) or fans (de Jong et al. 2009) pointing toward a central region of homogeneous isotropic turbulence (HIT). That HIT region, however, is typically limited under such symmetric forcing, often smaller than the integral length scale of the flow, while the configuration prohibits the investigation of turbulence in the vicinity of boundaries, which is of interest in floating particle transport. For boundary-related problems such as mixing and entrainment across interfaces (Thompson and Turner 1975; Hopfinger and Toly 1976) and turbulence near free surfaces (Brumley and Jirka 1987; McKenna and McGillis 2004), "stirred tank" designs with oscillating grids have been employed, where wakes from the grid interact to produce HIT sufficiently away from it. However, such systems often exhibit non-negligible secondary motions and inhomogeneities in the flow (McKenna and McGillis 2004). Improvements in homogeneity and isotropy, as well as higher Reynolds numbers, have been achieved when employing a spatio-temporally varying, randomly actuated synthetic jet array (RASJA) instead (Variano and Cowen 2008). Applications of RASJA systems in recent literature include the investigation of the influence of a free surface on the subsurface turbulent flow (Variano and Cowen 2008), later extended to scalar transport near a free surface (Variano and Cowen 2013), and turbulence above solid boundaries with the array operated in an inverted configuration (Johnson and Cowen 2018). The random nature of the forcing and the relatively large degrees of freedom enabled by the RASJA allow the flow properties to be tailored while maintaining a negligible mean flow (Pérez-Alvarado et al. 2016). Leveraging this capability and the RASJA's suitability for studying near-boundary phenomena, our study was performed in a facility inspired by its design.

As discussed earlier, investigations of free surface turbulence and floating particle dynamics have largely been confined to turbulence boxes and open-channel flows. Within this body of work, the surface flow itself has been primarily studied in the latter, through both experiments (Komori et al. 1982; Rashidi 1997; Kumar et al. 1998) and numerical simulations (Banerjee 1994; Pan and Banerjee 1995; Nagaosa 1999; Lovecchio et al. 2003). A link between the turbulent structures originating at the channel bottom and those present *along* the free surface was emphasized in these studies. Recently, Aarnes et al. (2025) reinforced this view analyzing conditional probabilities between free surface features and the subsurface flow in direct numerical simulation data of subsurface HIT–free surface interactions. However, Savelsberg and van de Water (2009), in an experimental open-channel flow study with turbulence generated by an active grid, reported a weak correlation between free surface indentations and the subsurface velocity field. They attributed the reduced correlation to the presence of random capillary gravity waves. Using a similar facility to Savelsberg and van de Water (2009), Bullee et al. (2024) observed that such waves exhibit correlations with their sources that are non-local in space and time. In contrast, the surface imprints of subsurface turbulent eddies are observed to be more localized (Muraro et al. 2021; Babiker et al. 2023), a difference that may have contributed to the weak correlation observed between the surface features and the subsurface flow in Savelsberg and van de Water (2009). Even in the regime of a relatively flat surface, which is of interest in our study, the nature of the surface flow has been the subject of ongoing debate in literature. In particular, for open-channel flows, earlier studies have reported the surface flow to be quasi-two-dimensional with prevalence of time persistent vortices at the surface (Pan and Banerjee 1995; Kumar et al. 1998), while others have highlighted its three-dimensional nature, supported by observations of vortex stretching at the free surface (Walker et al. 1996) and strong intermittency in floating particle accelerations (Li et al. 2025; Sanness Salmon et al. 2023). Support for the latter was further provided by experimental (Goldburg et al. 2001; Cressman et al. 2004) and numerical simulations (Eckhardt and Schumacher 2001) above HIT. These studies found the structure function at the surface to scale as for a three-dimensional flow with strong intermittency in the velocity and vorticity

differences and in the surface divergence. The nonzero value of the surface divergence arises from the 2*D* compressible nature of the surface: Upwellings and downwellings from the incompressible bulk flow appear as sources and sinks at the surface (Guo and Shen 2010; Ruth and Coletti 2024).

With respect to floating particle behavior, this 2*D* compressibility of the surface flow leads to clustering, as confirmed across a range of studies: experimental (Cressman et al. 2004; Larkin and Goldburg 2010; Qi et al. 2025; Li et al. 2025), numerical (Lovecchio et al. 2003; Chor et al. 2018) and modeling approaches based on surface ocean turbulence (Maalouly et al. 2023; Meacham and Berloff 2023). Initially distributed homogeneously, floating particles aggregate into sharp concentration fronts forming string-like distributions: fleeing upwellings (sources) and accumulating in downwellings (sinks). The degree of clustering, typically quantified in the literature using Voronoï tessellation, reaches values comparable to those of inertial particles in turbulence with a Stokes number of unity (Li et al. 2025). Furthermore, the clusters formed exhibit fractal-like scaling in both open-channel flows (Lovecchio et al. 2003) and surface flows above HIT (Larkin and Goldburg 2010). Chor et al. (2018) refined such associations of clustering with surface flow divergence, by performing large eddy simulations of the evolution of floater concentrations in the ocean mixed layer under free convection. They distinguished two types of preferential concentration, the primary being due to surface divergence, but happening immediately after initialization and being relatively short lived, and the secondary following at later stages and lasting much longer, attributed to floating particles becoming trapped within long-lived, surface-attached vortices. Using a kinematic flow model designed to resemble turbulent oceanic surface currents, Meacham and Berloff (2023) also investigated the temporal scales involved and found that time coherence in velocity fields led to enhanced particle aggregation rates, with larger, more coherent, and longer-lived clusters forming compared to an uncorrelated flow. Besides the surface flow, connections with the subsurface turbulence have also been identified, with clusters shown to exhibit length and time scales comparable to the integral scale of the flow (Qi et al. 2025; Li et al. 2025), again far exceeding those associated with surface divergence. Lovecchio et al. (2003) highlighted a possible dependence of clustering dynamics on the nature of the subsurface flow itself, observing slower cluster de-correlation times in an open-channel flow than those reported by Larkin and Goldburg (2010) for surface flow above HIT.

From the above, it becomes clear that subsurface turbulence, surface flow structures and floating particle behavior are intimately linked, and yet many open questions remain in associating the clustering temporal and spatial scales to specific flow events. In particular, the sensitivity of clustering dynamics to the underlying turbulence intensity as well as the combined roles of vorticity, surface divergence, and capillarity—each operating at different spatial and temporal scales—in such phenomena, remains relatively obscure. From a methods perspective, high-fidelity simulations often employ a point-particle approach that neglects interparticle interactions, while surface forces arising from capillary interactions, a mechanism particularly relevant at free surfaces (Protière 2023), are also commonly not accounted for. While experimental setups do not suffer from such limitations, concurrent measurements of the surface flow field while simultaneously tracking floating particles are challenging and thus have been scarce. To this end, in the current study, we carry out measurements of a relatively flat free surface flow field laden with floating particles (hereafter termed "floaters") above a nearly homogeneous turbulent flow of varying intensity. The surface flow field is measured using planar particle image velocimetry (PIV) while simultaneously tracking floaters using particle tracking velocimetry (PTV). We demonstrate the applicability of this technique in investigating the clustering of floating particles for different turbulence levels.

The manuscript is organized as follows. Section 2 includes details of the experimental setup, the phase discrimination (section 2.1), and velocity estimation (Sect. 2.2). The surface flow statistics are characterized in Sect. 3.1 while the clustering statistics of floaters are characterized in Sect. 3.2. Preliminary results of flow–floater interactions are discussed in Sect. 3.3 with conclusions and future work presented in Sect. 4.

2 Experimental setup

Experiments are performed in the TRACKqua facility of the Laboratory for Aero and Hydrodynamics at TU Delft. The facility (see Fig. 1), a glass cuboidal tank of cross section 1.2×1.2 m^2 and height 1.4 m, houses a pump array located at the base of the tank. The pump array consists of 100 submersible pumps (Albin bilge pump 32 L/min at 12 Volts) placed in a 10×10 cartesian grid configuration with a spacing of 9.5 cm in both horizontal directions (x and y). Each submersible pump directs a jet toward the free surface by drawing water radially from its base and ejecting it from a nozzle located 19 cm from the base of the pump. Since the suction and ejection of water from the pumps take place simultaneously, there is no net flux of mass introduced. 3*D*-printed 90° elbows with a nozzle diameter of 14 mm (denoted as d) and a length of $7.5d$ are attached to the pumps. This length is adequate to straighten the flow and mitigate any secondary swirling effects due to the elbow.

The pumps are controlled through ethernet-based solid-state relays (ETH8020 by Devantech) that are triggered through a custom MATLAB code. Upon activation, each

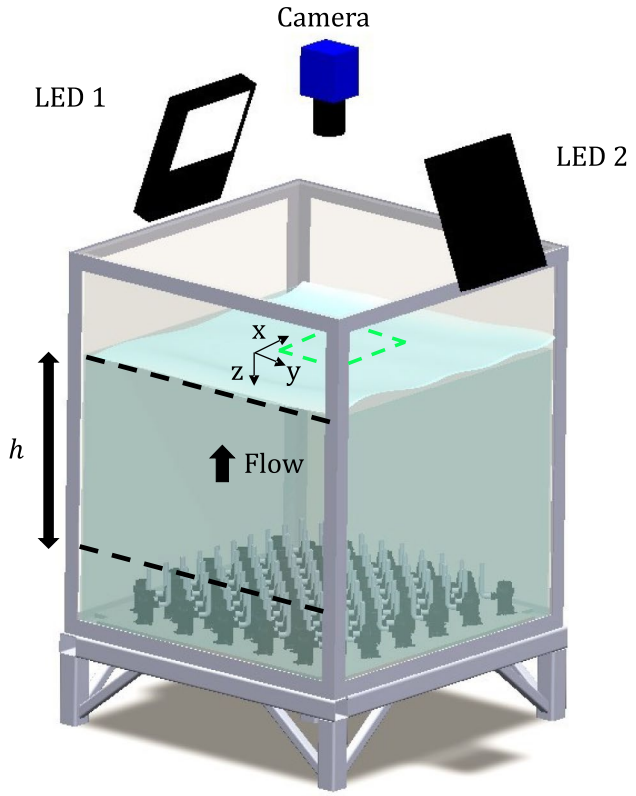

Fig. 1 A model of the experimental facility TRACKqua with a pump array located at the base of the tank which drives turbulence toward the free surface. The green dashed rectangle represents the field of view captured (27×32 cm^2 in x and y directions, respectively). h is the distance between the free surface and the outlet of the pump nozzles

relay completes a circuit that delivers 12 Volts at 1.8 Amps to the designated pump. The jet firing pattern is governed by the sunbathing algorithm Variano and Cowen (2008) which introduces spatial and temporal randomness to the firing sequence. Pérez-Alvarado et al. (2016) showed that this algorithm can generate flows closely approximating zero-mean flow HIT at relatively high Reynolds numbers outperforming other algorithms in the literature. In the sunbathing algorithm, each jet operates independently switching on and off repeatedly, with the durations of these periods sampled from Gaussian distributions characterized by their respective means and standard deviations (μ_{on}, μ_{off} and $\sigma_{on}, \sigma_{off}$, respectively). The source fraction ϕ, which relates μ_{on} and μ_{off} ($\phi = \mu_{on}/(\mu_{on} + \mu_{off})$), controls the momentum input to the flow and hence the turbulence intensity. Experiments in the current study are performed with $\mu_{on} = 0.7$ sec and $\phi = 40$ %, which were found to be optimal in the mixing of the subsurface flow and minimizing free surface imprints by individual jets.

In the current study, the distance of the free surface from the pump nozzle exit (h; see Fig. 1) is varied from 1 m to 0.6 m (cases C1 to C4; see Table 1) to achieve different flow conditions at the free surface (see Table 2 and section 3.1 for discussion). Specifically, the turbulence level is varied by changing h and its effect on the clustering of floaters is characterized. We perform both single-phase (using only surface tracers) and two-phase (with both surface tracers and floaters) measurements for each case (C1–C4). In addition, we compare the floater clustering statistics in cases C1–C4 to a case without a subsurface flow (case No flow (NF)). For all the cases studied, the free surface deformations are minimal with negligible wave generation, consistent with the small values of the Froude ($Fr = u_{rms}/\sqrt{g\mathcal{L}_{xx}} \sim \mathcal{O}(10^{-2})$) and Weber ($We = \rho u_{rms}^2 \mathcal{L}_{xx}/\sigma \sim \mathcal{O}(10^{-2})$) numbers (estimates from the lowest h case where most deformations expected), also supported by visual observations. Here, u_{rms} is the root-mean-square (rms) velocity fluctuation, $\mathcal{L}_{xx}$ is the integral length scale (discussion of estimates in section 3.1), and ρ and σ are the mass density and surface tension of water, respectively.

Table 1 Experimental cases investigated with associated acquisition parameters (single-phase flow). h is the distance between the free surface and the pump nozzle exit. f_{ls} and f_{hs} are the image acquisition rates, while N_{ls} and N_{hs} are the number of images acquired for statistically independent and time-resolved statistics, respectively

Case	h (m)	f_{ls} (Hz)	f_{hs} (Hz)	N_{ls}	N_{hs}
C1	1	1.5	10	2500	6000
C2	0.8	1.5	14	2500	6000
C3	0.7	1.5	17.5	2500	8000
C4	0.6	1.5	20	2500	9000

A single-camera planar PIV setup is utilized to measure the free surface flow field and track floaters simultaneously. The downward looking LaVision's Imager sCMOS CLHS camera (5 Mpix, 16-bit) captures a 27 (x) $\times$ 32 (y) cm^2 field of view (FOV) at a resolution of 8 pix/mm that is illuminated by two continuous LED panels (Noxion LED Floodlight 170 Watts). A 24 mm Samyang lens is fitted to the camera with the aperture opened completely ($f_\# = 1.4$) to minimize the focal depth (≈ 2 mm) and prevent imaging of flow tracers *below* the free surface. Owing to the minimal undulations of the free surface, any unwanted light reflections are effectively absent. The camera acquisition parameters for the single-phase flow measurements are provided in Table 1. Low-speed (f_{ls}, N_{ls}) and time-resolved (f_{hs}, N_{hs}) data are used to obtain statistically independent and time-resolved statistics, respectively, as presented in section 3.1. For the two-phase flow measurements, we perform 10 independent time-resolved runs for each case (using the same f_{hs} as shown in Table 1), acquiring approximately 8000 images per case for the floater clustering statistics presented in section 3.2. For the NF case, we acquire 3000 images at $f_{hs} = 1$ Hz.

For the free surface flow measurements, we seed the free surface using Polyamide tracers that have a mean diameter of 60 µm. To prevent tracer aggregation caused by surface tension, the tracers are wetted with a small amount of surfactant (20 mL of Cospheric Tween 80 per 1 m^3 of water). Monodisperse polypropylene spheres of diameter $d_p = 2$ mm and specific gravity 0.87 are used as the floaters that are dispersed over the free surface using a custom-made seeding grid. The seeding grid consists of two perforated plates placed just above the free surface. The floaters are placed in the holes of the first plate; they are kept in place by an initial misalignment of the two plates and can be seeded into the flow when the plates are offset such that their perforations align, providing a repeatable seeding method. The volume of submergence of the floaters in water varies between $88 - 92$ %. The change in floater submergence due to the small concentration of surfactant used is expected to be negligible (less than 5 %). The relevant floater characteristics with respect to the single-phase flow scales (for cases C1–C4) are as follows: $d_p/\mathcal{L}_{xx} \approx 0.05 - 0.06$, $d_p/\eta \approx 2.5 - 3.5$ and Stokes number $St_\eta = \tau_p/\tau_\eta \approx 0.25 - 0.5$, where η and τ_η are the Kolmogorov length and time scales, respectively, and τ_p is the floater response time that is estimated assuming the floater is completely submerged in water. For all the cases studied, the floaters remain at the free surface, a characteristic commonly governed by the floatability parameter $\beta = u_t/u_{rms}$, where u_t is the terminal rise velocity of the particle (Chor et al. 2018) (here, $\beta \approx 8$). To characterize the influence of turbulence levels on floater clustering, the flow tracers and floaters must first be distinguished, followed by identification of floater clusters and their classification.

2.1 Phase discrimination and cluster classification

The continuous and dispersed phases are distinguished by exploiting the size disparity ($\mathcal{O}(10^2)$) and number density ($\mathcal{O}(10^2)$) between the tracers and floaters. Figure 2 shows an outline of the steps, and Fig. 3 provides a visual illustration of the process.

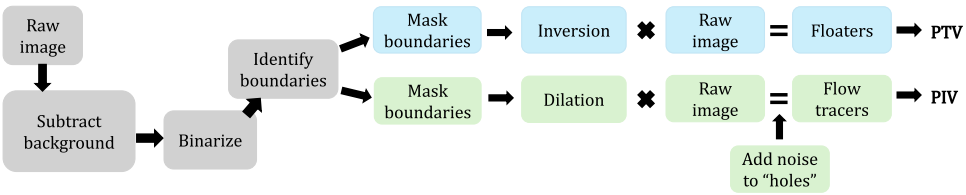

Fig. 2 Steps involved in the phase discrimination between the continuous and dispersed phases

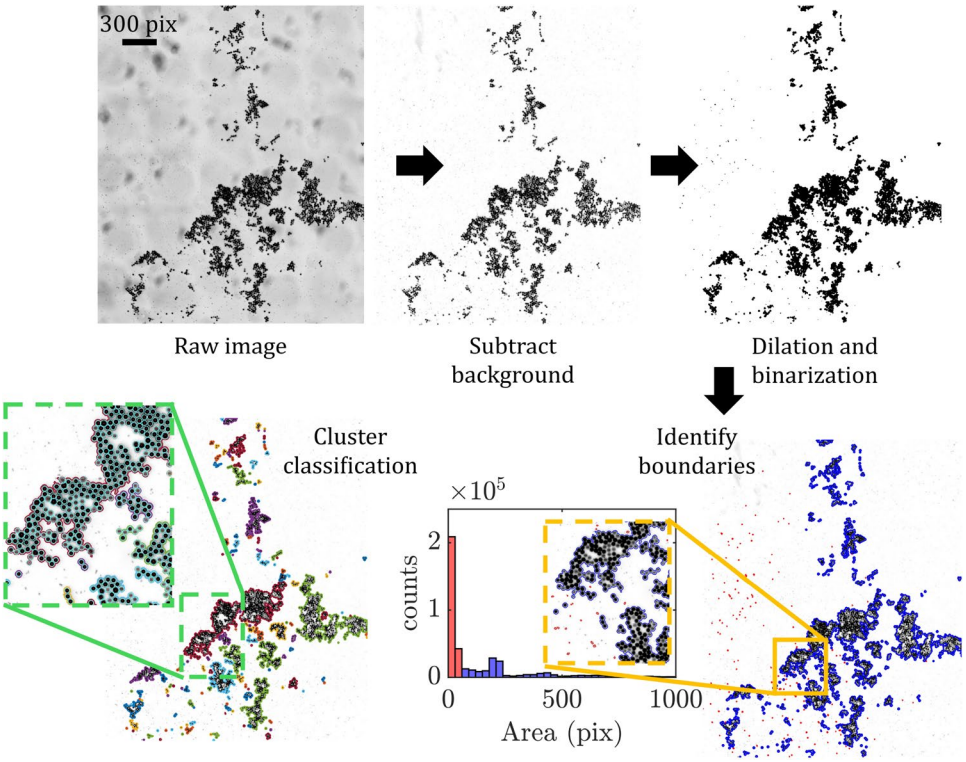

Fig. 3 Visual illustration of the phase discrimination process between the continuous (flow tracers) and dispersed phase (floaters) up to the "Identify boundaries" step in Fig. 2. Also shown is a histogram of areas (pix) (ensemble over all instantaneous images in a dataset) enclosed within the detected boundaries enabling segregation between tracers (marked in red) and floaters (marked in blue). Individual floaters can then be identified (see inset of "Cluster classification" step; individual floaters marked in cyan) within the floater boundaries enabling cluster classification based on the number of floaters contained (shown in different colored boundaries)

Initially, a background with no tracers or floaters present is subtracted from the raw images. This removes image features that are not relevant such as the pumps in the background thereby improving contrast between the tracers and floaters (see "Subtract background" step in Fig. 3). This is followed by a morphological dilation. To facilitate the identification of floater boundaries ("Identify boundaries" step in Fig. 3, blue outlines) and their segregation from tracers, binarization is first implemented as a preprocessing step. As a result, high-intensity regions (floaters) are isolated from the relatively low-intensity tracers (see figure 3 where intensity increases from white (low) to black (high)). The boundaries of these high-intensity regions are then identified using MATLAB's in-built Moore–neighbor tracing algorithm which traces closed contours based on pixel connectivity. Binarization helps in significantly reducing the tracer contributions to the phase segregation process due to their lower intensity. However, some tracers may not be completely removed at this stage. A histogram of areas enclosed within the detected boundaries provides a secondary means for further discrimination (see Fig. 3). The histogram exhibits a prominent peak at relatively smaller areas and a tail extending toward relatively larger areas. The former corresponds primarily to tracer boundaries characterized by relatively high number density and smaller sizes (marked in red). On the other hand, the latter corresponds to boundaries of floater clusters of different sizes characterized by relatively lower number density and larger areas (marked in blue). This distinction, based on size disparity and number density obtained from the histogram of areas enclosed within the detected boundaries, is used to separate the continuous phase (flow tracers) from the dispersed phase (floaters). By subsequently utilizing the identified dispersed phase boundaries as masks in the raw images, the floaters are extracted through inversion. On the other hand, to isolate the flow tracers, the masks are first enlarged by dilation to remove any halos present around the floaters. The dilated masks are then multiplied with the raw image resulting in a tracer-only image with "holes" left by the masks containing the position of the floaters. The latter are filled with noise with an amplitude comparable to the background noise of the raw image. This procedure is applied to the entire image series to yield the discriminated phases.

The floater-only images are utilized to identify individual floater centroids. This is done using MATLAB's built-in Circular Hough transform algorithm, which can be implemented and tuned relatively easily facilitated by the monodispersity of the floaters. Briefly, the algorithm detects circles by mapping edge pixels located at a distance of approximately one floater image radius, into a parameter space of possible center coordinates. A local maxima in this space corresponds to circle centers (i.e., floater centroids). Sometimes, false positives occur. This includes overlapping circles when floaters cluster together, or circle centroids identified at floater edges due to uneven illumination. By ensuring that detected centroids lie within high-intensity regions, and then applying a minimum distance threshold between centroids equal to d_p, these false positives are eliminated. The identified individual floaters are then employed along with the previously demarcated dispersed phase boundaries (identified in the "Identify boundaries" step, outlined in blue in Fig. 3) to carry out cluster classification (see inset of "Cluster classification" step in Fig. 3). This is done by counting the number of floaters within each identified boundary. In what follows, we define a cluster as *two or more* floaters within a closed boundary. We will utilize this classification to analyze cluster size distributions and their evolution under different turbulence levels, with estimation of velocities discussed next.

2.2 Velocity estimation

2.2.1 Particle image velocimetry

Velocity fields of the free surface flow for both single (tracer-only) and two-phase (tracers and floaters) flow cases are obtained through a multi-pass cross-correlation process of the raw and phase-discriminated tracer images, respectively, using Davis 11.0.0. The final window size is 96×96 pix with an overlap of 75 %, the latter selected to improve sampling in regions of high spatial velocity gradients (Tokgoz et al. 2012), such as those associated with surface divergence and vorticity (for example, see Fig. 6 and section 3.1 for discussion). The final vector spacing is 3 mm. The universal median test is used to validate the vectors and eliminate any spurious ones (Westerweel and Scarano 2005), which accounted for less than 5 % of the total.

2.2.2 Particle tracking velocimetry

The identification of individual floaters (single or in clusters), along with their relatively low number density ($\mathcal{O}(10^3)$), enables their time tracking. When this is coupled with velocity fields of the free surface flow (obtained through PIV), cluster formation and evolution of floaters can be analyzed, an area of research within particle-laden turbulent free surface flows that remains largely unexplored. To this end, we implement an in-house custom PTV algorithm to track floater centroids between frames (see Fig. 4, left). It combines a nearest neighbor approach (Malik et al. 1993) with a multi-frame strategy (Nishino et al. 1989; Hassan and Canaan 1991; Oulette et al. 2006). The algorithm first identifies all floater centroids at time t. To estimate their floater displacements at time $t + dt$, a circular search radius based on a representative average floater displacement between

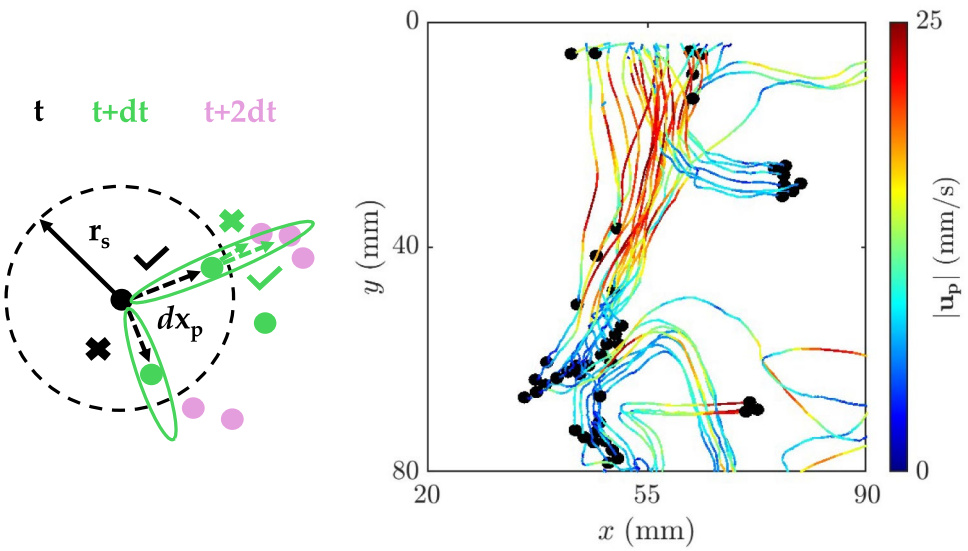

Fig. 4 Left: Schematic of the PTV algorithm. Right: A representative instantaneous snapshot of floater velocity trajectories (tracked over 50 frames) colored by their instantaneous velocity magnitudes ($|\mathbf{u_p}|$). Initial floater positions are marked by black filled circles

frames ($r_s = d_p$) is defined. Floaters found within that radius at time $t + dt$ are then assumed to be possible matches. Subsequently, a refined search, using an elliptical search area, is made for all of them for time $t + 2dt$. The ellipse is projected along the floater's displacement vector $d\mathbf{x_p}$ from the previous time step (t to $t + dt$), its semi-major axis corresponding to $|d\mathbf{x_p}|$ and its semi-minor axis to $d_p/2$. Using an elliptical search radius is beneficial when displacements exceed d_p and in reducing the potential number of matches, the latter particularly useful in tracking floaters within clusters. The best trajectory is selected by matching the floater to its nearest neighbor (if there is one) and minimizing the angle between the two displacement vectors ($t \rightarrow t + dt$ and $t + dt \rightarrow t + 2dt$). This criterion prevents false positives (if any) and is effective for the high temporal resolution available. Finally, this procedure is repeated for subsequent time steps, $t + 3dt, t + 4dt$ and so on. In every independent measurement run, we track on average 2000 floaters with about 10 % of trajectories rejected. Different paths taken by floaters (either single or in clusters) as they navigate through different flow regions can be observed in an instantaneous snapshot of floater velocity trajectories taken over 50 frames (see Fig. 4, right). As one would expect, floaters within clusters tend to move collectively (except in cluster forming/breaking events), exhibiting similar phases of acceleration and deceleration. Furthermore, these motions are well correlated with the curvature of the floater paths, information which can provide insight into dynamics of floaters within clusters.

As mentioned previously, the focus of the current study lies in the clustering statistics of floaters under varying turbulence levels. Developing the tools for simultaneous free surface flow measurements and floater tracking as described here additionally allows us to analyze formation and evolution of clusters associated with specific flow features; even though a detailed analysis of such flow–floater interactions is reserved for future work, some representative examples will also be highlighted here, after the results on the clustering statistics (see section 3.3).

3 Results

3.1 Flow statistics

Based on the PIV analysis on the tracer images described above, the surface flow statistics are first presented here. In what follows, we denote the components of the instantaneous flow velocity vector $\mathbf{u}$ by u and v in the x and y directions, respectively. In RASJA facilities such as the one used here, the strength of the mean flow created will depend on the actuation parameters employed. For the parameters used here (minimizing free surface deformations) and for very long averaging times (2 hours), the mean flow is between $7 - 30\%$ of the rms fluctuations (see Appendix for a detailed quantification of the mean and the discussion below for the rms calculation). Long times are needed to average out slowly evolving, large-scale flow patterns that are a result of the random nature of actuation and exist in addition to turbulent fluctuations. To ensure that these slowly evolving patterns do not contribute to the turbulence statistics, instead of a long averaging time, we compute spatially averaged velocities ($\overline{u}$ and $\overline{v}$) for every instantaneous velocity field instead. Subsequently, we subtract them from u and v, respectively, to get the instantaneous velocity fluctuations (u' and v', respectively):

$$u_i'(x,y,t) = u_i(x,y,t) - \overline{u_i}(t) = u_i(x,y,t) - \frac{1}{IJ}\sum_{x=1}^{I}\sum_{y=1}^{J} u_i(x,y,t) \quad (1)$$

Here, i is the component of velocity considered (u or v) and I and J are the number of velocity vectors in x and y directions, respectively. Subsequently, the rms velocity fluctuations are found by $u_{i,rms} = \sqrt{\frac{1}{N}\sum_{t=1}^{N} u_i'^2}$, where N is the number of ensembles.

As mentioned in section 2, four different cases were studied (C1–C4) based on a decreasing nozzle-to-free surface distance, h; statistics of the single-phase (no floaters) free surface turbulent flow for each of them are summarized in Table 2. These statistics were not altered in the presence of floaters (two-phase flow), and thus, those are omitted. With decreasing h, the turbulence level is observed to increase. This is reflected in the increase of u_{rms} and v_{rms} by approximately 50 % from C1 to C4 (and a resulting range of Taylor-scale Reynolds number $Re_\lambda = 72 - 101$). In addition, the rms free surface normal vorticity ($\omega_{z,rms}$) and the rms surface divergence ($(\nabla \cdot \mathbf{u})_{rms}$; surface divergence defined as $\nabla \cdot \mathbf{u} = \partial u/\partial x + \partial v/\partial y$) also increase, exhibiting a relatively greater change compared to the rms velocity fluctuations (about 62 % in $\omega_{z,rms}$ and 150 % in $(\nabla \cdot \mathbf{u})_{rms}$ from C1 to C4).

The longitudinal integral length scales in the x and y directions ($\mathcal{L}_{xx}$ and $\mathcal{L}_{yy}$, respectively) and the Taylor microscale (λ) are computed from the spatial autocorrelation function of the velocity fluctuations,

$$\rho_i(\mathbf{r}) = \frac{\overline{u_i'(\mathbf{x})\, u_i'(\mathbf{x}+\mathbf{r})}}{\overline{u_i'^2}}, \tag{2}$$

where $\mathbf{r}$ signifies the separation vector and i the component of velocity considered (u or v). Subsequently, $\mathcal{L}_{xx}$ and $\mathcal{L}_{yy}$ can be found by

$$\mathcal{L}_{ii} = \int_0^\infty \rho_i(\mathbf{r}) d\mathbf{r} \tag{3}$$

while λ is found by fitting a parabola of the form $\rho_i(r) = 1 - (1/2)(\mathbf{r}^2/\lambda^2)$ near the origin of $\rho_i(\mathbf{r})$ (Nieuwstadt et al. 2015), which is later used to normalize the scales of ω_z and $\nabla \cdot \mathbf{u}$. The FOV employed here is sufficiently large to resolve the integral length scale such that estimations of $\mathcal{L}_{ii}$ are not biased ($\approx 8\mathcal{L}_{ii}$). $\mathcal{L}_{xx}$ and $\mathcal{L}_{yy}$ are found to be of the order of d, consistent with previous observations in jet-stirred turbulence (Carter et al. 2016; Bang and Pujara 2023). The level of anisotropy observed in all cases here ($\mathcal{L}_{xx}/\mathcal{L}_{yy}$) is comparable to that of jet-stirred turbulence tanks without symmetric forcing (Variano and Cowen 2008; Johnson and Cowen 2018).

Spatial gradients in the flow, specifically those associated with vorticity and surface divergence, are important physical mechanisms in floater clustering and breakup (Chor et al. 2018; Qi et al. 2025). While areas of mean flow convergence could, in principle, promote floater aggregation, the spatial gradients associated with the mean flow required to affect floater clustering act over time scales much longer than the clustering time scales linked to spatial gradients associated with turbulent fluctuations (see discussion in Appendix). Furthermore, the trends observed in the temporal evolution of floater clustering and its associated time scales discussed in section 3.2 remain quantitatively consistent across different realizations despite variations in the mean flow strength and direction among realizations, indicating repeatability of the clustering statistics (see Fig. 15 in Appendix). Thus, while a non-negligible mean flow is present, it does not play a significant role compared to turbulent fluctuations in the clustering dynamics of floaters.

The normalized probability density functions (pdf) of u' and v' for all the cases are shown in Fig. 5(a) and (b). The pdfs of u' and v' exhibit a negligible skewness (Sk $\approx \mathcal{O}(10^{-2})$) and a kurtosis (Ku) of approximately 3.7 indicating a higher probability of extreme velocity fluctuations compared to a Gaussian distribution, a characteristic typical of a fully developed turbulent flow (Mouri et al. 2002; Li and Meneveau 2005; Ruth and Coletti 2024). These values are consistent with similar zero-mean flow HIT experimental setups (Variano and Cowen (2008): Ku ≈ 4; Carter et al. (2016): Ku ≈ 3.2; Bang and Pujara (2023): Ku ≈ 3.9), where velocity fluctuations were measured in the homogeneous subsurface region. Furthermore, the collapse of the pdfs for different cases (when normalized by their rms values) suggests similar statistical distributions of the velocity fluctuations across changing turbulence intensities.

As discussed in section 1, both experimental (Cressman et al. 2004; Qi et al. 2025) and numerical studies (Lovecchio et al. 2003; Chor et al. 2018) reported velocity gradients on the free surface to play an important role in the clustering

Table 2 Single-phase turbulent flow statistics measured at the free surface for different cases. $\omega_{z,rms}$ and $(\nabla \cdot \mathbf{u})_{rms}$ are the rms free surface normal vorticity and surface divergence values. $\mathcal{L}_{xx}$ and $\mathcal{L}_{yy}$ are the integral length scales in the x and y directions, respectively. λ and λ_T are the Taylor microscale and timescales, respectively

Case	u_{rms} (mm/s)	v_{rms} (mm/s)	$\boldsymbol{\omega_{z,rms}}$ (s^{-1})	$\boldsymbol{(\nabla \cdot \mathbf{u})_{rms}}$ (s^{-1})	$\boldsymbol{\mathcal{L}_{xx}}$ (mm)	$\boldsymbol{\mathcal{L}_{xx}/\mathcal{L}_{yy}}$	$\boldsymbol{\lambda}$ (mm)	$\boldsymbol{\lambda_T}$ (sec)	Re_λ
C1	4.3	4.2	0.59	0.14	36.55	1.02	15.99	1.26	72
C2	4.3	4.4	0.60	0.25	33.59	0.98	14.69	0.92	68
C3	5.3	5.4	0.79	0.37	32.32	0.98	13.97	0.59	77
C4	6.5	6.6	0.96	0.36	34.08	1.01	14.95	0.72	101

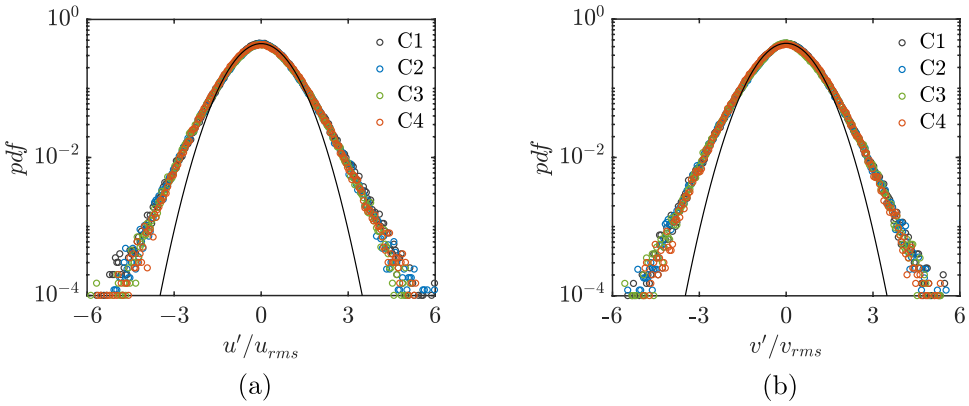

Fig. 5 Pdf of velocity fluctuations (a) u' and (b) v' normalized by their respective rms values

of floating tracers. Specifically, ω_z and $\nabla \cdot \mathbf{u}$, distinct in both their spatial extent and temporal duration (Qi et al. 2025), have been hypothesized to imprint their scales on the clusters formed. In the present study, different spatial scales of ω_z and $\nabla \cdot \mathbf{u}$ can be qualitatively observed in representative instantaneous fields (Case C4) shown in Fig. 6.

The surface divergence field displays patches of sources ($\nabla \cdot \mathbf{u} > 0$) and sinks ($\nabla \cdot \mathbf{u} < 0$) that occur at relatively smaller scales than the vorticity events. As we will show in what follows, this is not only instantaneously but also statistically true and is consistent with previous experimental (Qi et al. 2025) and numerical (Shen et al. 1999; Herlina and Wissink 2019) studies, highlighting that the length scales of the surface divergence field are smaller than those of the vorticity field, with sources ($\nabla \cdot \mathbf{u} > 0$) surrounded by sinks ($\nabla \cdot \mathbf{u} < 0$), and vice versa. Sources arise from upward-moving fluid parcels in the subsurface that diverge horizontally as they approach the free surface, producing upwelling boils or splats; sinks arise from fluid parcels converging near the surface and being redirected downward, producing downwellings or antisplats (Pan and Banerjee 1995; Perot and Moin 1995; Shen et al. 1999; Ruth and Coletti 2024). Upwellings or downwellings are generally characterized by regions where $\nabla \cdot \mathbf{u}$ is relatively large in magnitude and long-lived (Banerjee 1994; Ruth and Coletti 2024; Qi et al. 2025). We note that a rigorous quantification of splats and antisplats was provided by Shen et al. (1999), who defined them as large positive (negative) values of $\nabla \cdot \mathbf{u}$ when normalized by the square root of the TKE and accompanied by small horizontal velocities at the free surface. In the present

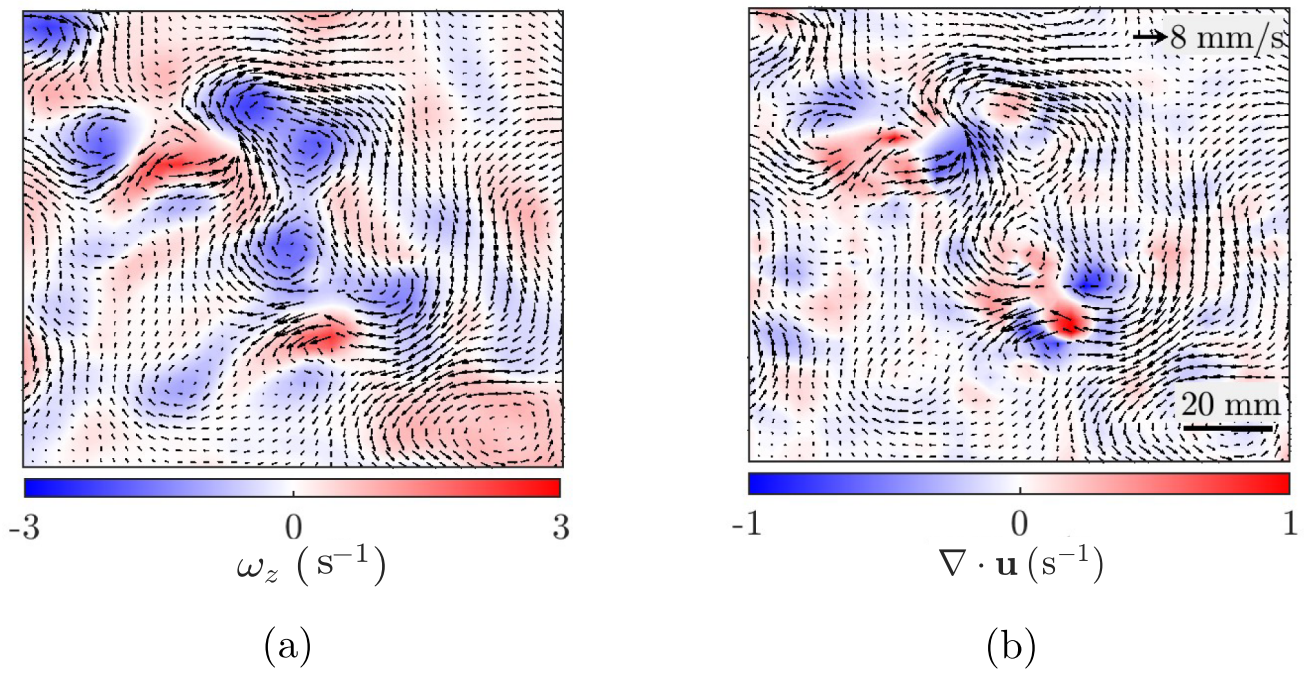

Fig. 6 Representative instantaneous snapshots of (**a**) vorticity (ω_z) and (**b**) surface divergence ($\nabla \cdot \mathbf{u}$) fields

study, for clarity, we refer to $\nabla \cdot \mathbf{u} > 0$ as positive surface divergence and $\nabla \cdot \mathbf{u} < 0$ as negative surface divergence. The vorticity field features elongated regions of both positive and negative vorticity, along with circular areas of high magnitude irrespective of sign, the latter typical imprints of surface-attached vortices (Banerjee 1994; Muraro et al. 2021; Babiker et al. 2023; Aarnes et al. 2025). These aspects of spatial coherence in addition to the variation of $\omega_{z,rms}$ and $(\nabla \cdot \mathbf{u})_{rms}$ with turbulence level (see Table 2) are expected to influence floater behavior.

The distributions of ω_z and $\nabla \cdot \mathbf{u}$ (Fig. 7(a) and (b), respectively) broaden from C1 to C4 (increasing turbulence activity). When normalized by their respective rms values, ω_z and $\nabla \cdot \mathbf{u}$ (Fig. 7(c) and (d), respectively), they exhibit long tails reflecting the strong intermittency in the surface flow, in line with previous observations from both numerical (Eckhardt and Schumacher 2001) and experimental (Cressman et al. 2004; Qi et al. 2025) studies. Furthermore, both ω_z and $\nabla \cdot \mathbf{u}$ exhibit symmetric distributions, the latter indicating that the occurrence of positive and negative surface divergence events are equally probable, consistent with previous observations (Qi et al. 2025).

As observed in Fig. 6, the spatial scales associated with ω_z and $\nabla \cdot \mathbf{u}$ differ, and these differences are expected to play a role in the formation and spatial characteristics of the floater clusters. To this end, we quantify their length scales through the spatial autocorrelation (vorticity: $\rho_\omega\,(r)$ and surface divergence: $\rho_{\nabla\cdot\mathbf{u}}\,(r)$, where r is the separation vector) which is shown in Fig. 8(a) and (b). The following observations can be made. First, no discernible differences in spatial extent are observed across cases C1–C4 for either ω_z or $\nabla \cdot \mathbf{u}$ with the Taylor microscale providing a reasonable collapse of $\rho_\omega\,(r)$ and $\rho_{\nabla\cdot\mathbf{u}}\,(r)$. Second, $\nabla \cdot \mathbf{u}$ exhibits a relatively smaller length scale ($\approx 0.5\lambda$) compared to ω_z ($\approx 1\lambda$), aligning with visual observations of representative instantaneous fields in Fig. 6. Beyond $\approx 1\lambda$ (see Fig. 8(a)), $\rho_\omega\,(r)$ drops to zero while $\rho_{\nabla\cdot\mathbf{u}}\,(r)$ exhibits a negative correlation (see Fig. 8(b)) instead. The latter occurs because, statistically, regions of positive surface divergence ($\nabla \cdot \mathbf{u} > 0$) are always surrounded by regions of negative surface divergence ($\nabla \cdot \mathbf{u} < 0$), and vice versa, in accordance with the conservation of mass.

In addition to their differing spatial extents, their temporal durations have also been found to be distinct (Qi et al. 2025), an aspect that can in turn affect the temporal evolution of clusters. In our study, the smaller spatial extent of $\nabla \cdot \mathbf{u}$ is corroborated by its relatively shorter temporal correlation ($\approx \lambda_T$) when compared to ω_z (see Fig. 8(c) and (d)). The latter exhibits relatively longer lifetimes ($\approx 4\lambda_T$) and is comparable to the integral timescale ($\mathcal{T}_\mathcal{L}$) consistent with recent experimental observations of Qi et al. (2025). This suggests that vortical features at the free surface are more time

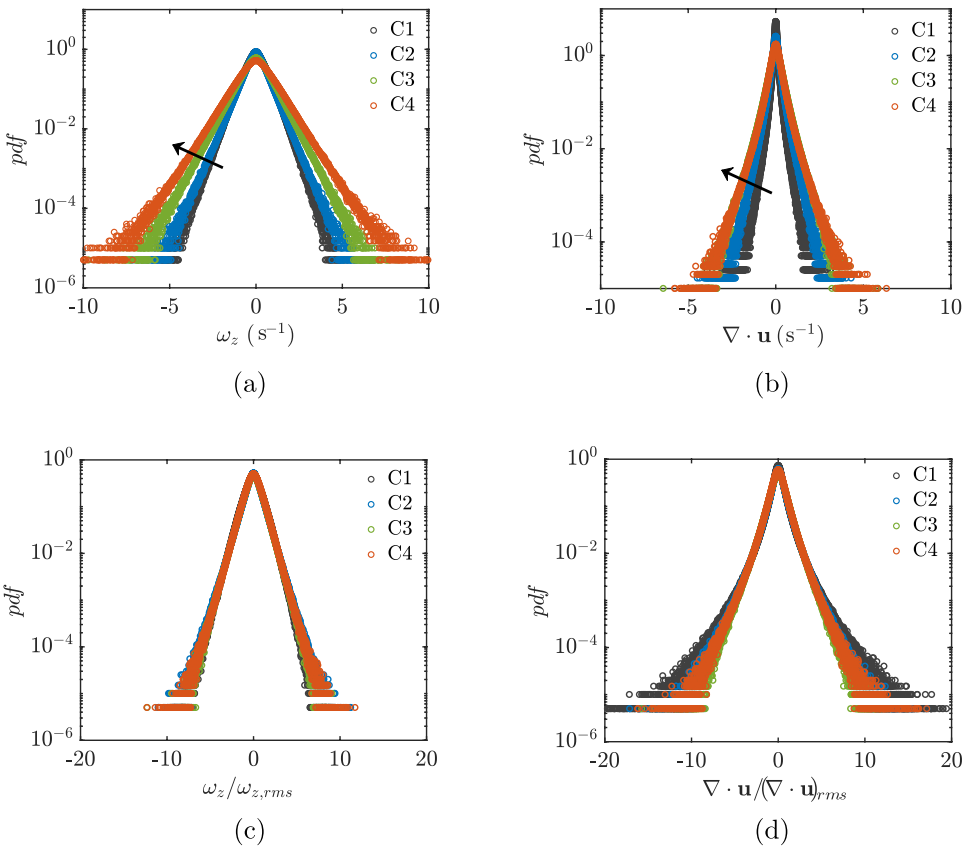

Fig. 7 Pdf of the free surface normal vorticity (a,c) ω_z and (b,d) surface divergence $\nabla \cdot \mathbf{u}$ in both dimensional and non-dimensional (normalized by respective rms values) forms for all the cases. The arrow in (a) and (b) shows increasing amplitude of ω_z and $\nabla \cdot \mathbf{u}$ with decreasing h

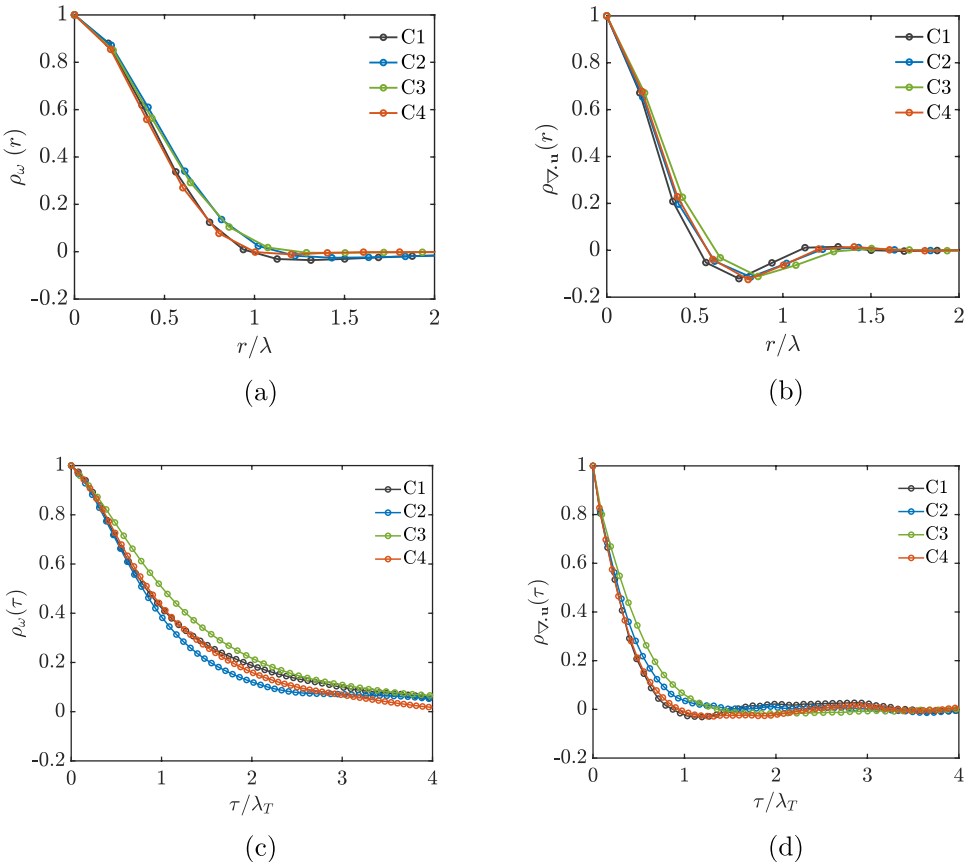

Fig. 8 Spatial autocorrelation of (a) ω_z and (b) $\nabla \cdot \mathbf{u}$ as a function of the separation vector (r) normalized by the Taylor microscale (λ). Also shown is the temporal autocorrelation of (c) ω_z and (d) $\nabla \cdot \mathbf{u}$ as a function of time lag (τ) normalized by the Taylor timescale (λ_T)

persistent than what would be expected in a 3D turbulent flow (which would scale with the Kolmogorov timescale), as previously observed for free surface-attached vortices (Shen et al. 1999; Aarnes et al. 2025). Within the turbulence levels tested here, both the short-term effects of sources and sinks ($\nabla \cdot \mathbf{u}$) and the longer-term influence of persistent vortices are expected to shape the clustering behavior of floaters, with the latter analyzed in what follows.

3.2 Floater statistics

As discussed in section 1, particles confined to an air–water interface cluster due to their inability to follow fluid pathlines entering the bulk, that is, they probe a compressible field at the free surface. Features of the surface flow, distinct from those in an incompressible 3D turbulent flow, such as the presence of positive/negative surface divergence and long-lived surface vortices, can in turn have implications on the transport of floating particles and their clustering. Here, we discuss how the clustering behavior of floaters is affected by the varying turbulence levels. Specifically, the identification and classification of clusters (see section 2.1) allow us to analyze the cluster size distribution and its time evolution for different cases. Clustering of floaters brings about spatial inhomogeneity at the free surface, which we quantify here using the Voronoï diagram method (Monchaux et al. 2010). The latter is often employed in experimental (Sumbekova et al. 2017; Petersen et al. 2019) and numerical studies (Tagawa et al. 2012; Baker et al. 2017; Maalouly et al. 2023) to study clustering in particle-laden turbulent flows. This approach tessellates the domain into cells, each associated with a specific floater. The ensemble of points of a particular Voronoï cell is closer to the corresponding floater than to any other. In other words, smaller Voronoï cells (larger Voronoï cells) indicate the floaters are positioned closer (farther apart) relative to each other. An example of a tessellated, instantaneous field of floaters is shown in Fig. 9 (bottom row, middle panel).

We employ the Voronoï tessellation in a flow case (C4; other cases are similar and are omitted here for brevity) and the NF case to evaluate the floater's clustering behavior in each one (see red and black solid line, respectively, in Fig. 9). The spatial distribution of the floaters follows the uniform spacing of the seeding grid before release. Upon release, the floaters fall randomly onto the surface. At the start of image acquisition ($t = 0$) which occurs with a short delay after floater release (≈ 1 sec), floaters have already begun to cluster (see Fig. 9 bottom row, left). Thus, the pdf of the Voronoï cell areas (A_v, which is normalized by the

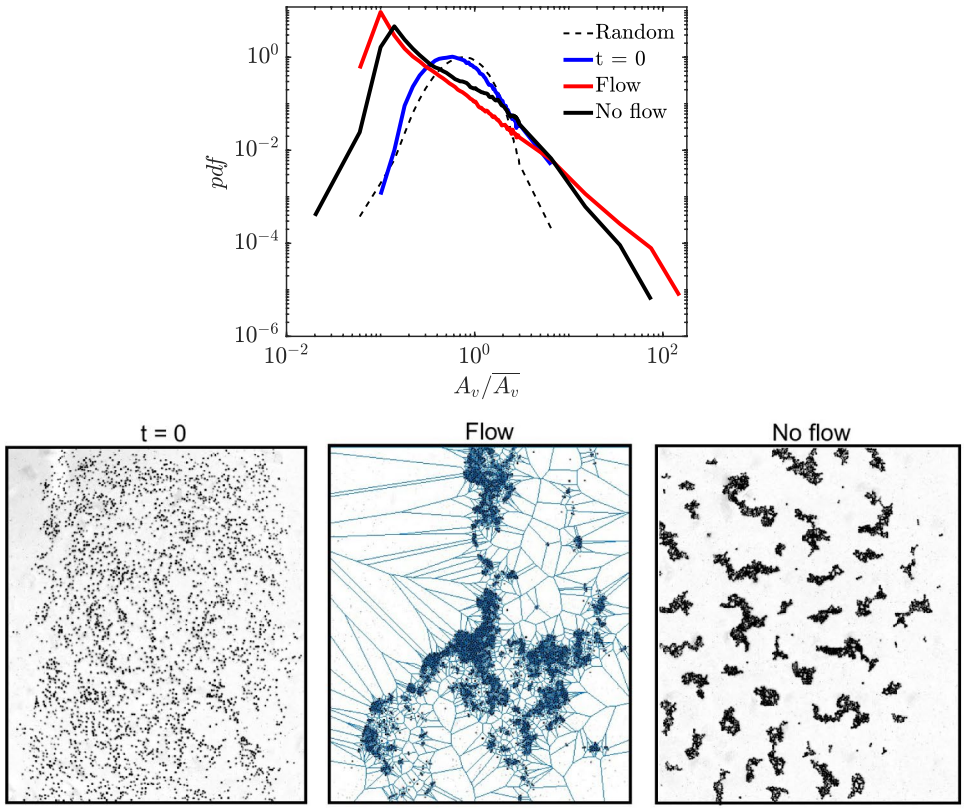

Fig. 9 Top: Pdf of the Voronoï cell areas (A_v) normalized by the mean Voronoï cell area of the domain ($\overline{A_v}$, computed at each time step) at time $t = 0$ (when the floaters are released; blue solid line) and at a later time t for cases C4 (Flow, red solid line) and no flow (black solid line). These are compared to a pdf for a set of floaters following a random Poisson process (black dashed line). Bottom row: Representative raw images at $t = 0$ (left panel) and at a later time t (during quasi-steady state, see Fig. 10) for the flow (middle panel with example Voronoï cells) and no flow (right panel) cases

mean cell area of the domain at each time instant $\overline{A_v}$) at $t = 0$, is quite similar but somewhat broader than that of a random Poisson process (Ference and Néda 2007) (see Fig. 9 top, blue solid: $t = 0$ and black dashed lines: "Random," respectively). At a later time, both the flow and the NF cases lead to floater clustering, which although spatially quite different (see Fig. 9 bottom row, middle, and right panels, respectively) results in similar pdfs of Voronoï cell areas (Fig. 9 top, red and black solid lines). Both of them exhibit a sharp peak and a broader tail when compared to the pdf at $t = 0$. A sharp peak at relatively small normalized Voronoï cell areas indicates an increased probability of smaller cell areas and thus floaters clustering together. A broader tail indicates an increased probability of larger cell areas due to the resulting voids. The degree of clustering, typically quantified using the standard deviation of A_v (σ_{A_v}) (Monchaux et al. 2010), relative to the pdf at $t = 0$ ($\sigma_{t=0}$), is found to be $\sigma_{A_v}/\sigma_{t=0} \approx 5$ for both the flow and NF cases, indicating a relatively high intensity of clustering. As a reference, inertial particles with a unit Stokes number in turbulent flow exhibit strong clustering, with reported ratios ranging from $1.5 - 3.5$ (Sumbekova et al. 2017; Baker et al. 2017; Petersen et al. 2019). While the pdf of the Voronoï cell areas provides a statistical measure of the local floater concentration, it inherently lacks global information of the clusters such as their size distribution and spatial arrangement across the FOV, aspects important to study clustering and its dynamics. In contrast, the ability to identify individual floaters and subsequently classify clusters based on the number of floaters included in each, as described earlier (see section 2.1), allows for a detailed insight into cluster distributions, their evolution, and their behavior under varying turbulence levels. Thus, in what follows we will use that kind of cluster classification for the rest of our analysis.

Given the above discussed clustering behavior of an initially random distribution of floaters in both cases with flow (C1 to C4) and without flow (NF) (also see supplementary movies), we first analyze the time scales involved in it. Specifically we track the number of floaters in clusters of any size at each time step ($N_c(t)$), normalized by the total number of floaters in the FOV, N, for all cases (Fig. 10). Normalization by N is essential to account for floaters entering/leaving the FOV due to the mean flow, the latter unavoidable in jet-stirred tanks. In cases with flow (C1 to C4), a plateau is observed in N_c/N where approximately 95 % of N cluster. This reflects a quasi-steady state characterized by a balance between cluster formation and breakup, with the time required to reach it ($t \approx 12$ (C4)–18 sec (C1); see dash-dotted lines of corresponding colors in Fig. 10) decreasing as the amplitude of ω_z and $\nabla \cdot \mathbf{u}$ (from C1 to C4, respectively) increases. On the other hand, in the NF case, a quasi-steady state is only reached when clusters continually form and grow until all the

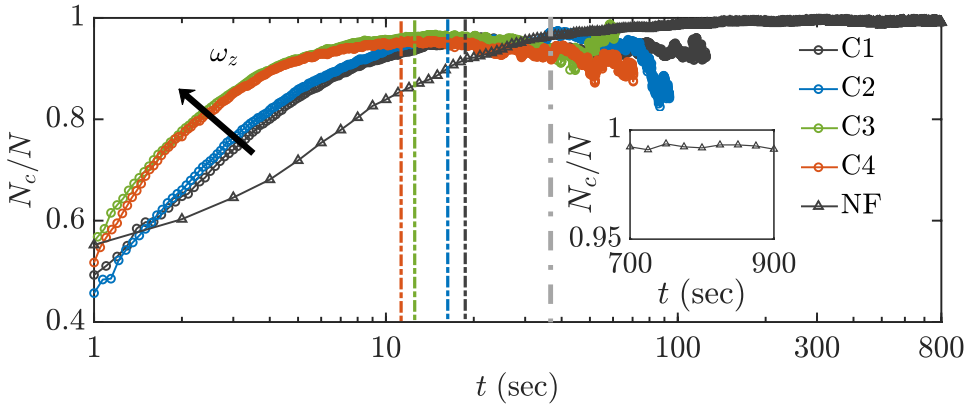

Fig. 10 Temporal evolution of the total number of floaters in clusters (N_c) normalized by the total number of floaters in the FOV (N) for different cases. Dash-dotted lines of corresponding colors indicates the approximate time at which 95 % of N cluster ($t \approx 12-18$ sec in cases C4–C1, respectively). Representative raw image of case C4 at an instant of time (gray dash-dotted line) during its quasi-steady state is shown in Fig. 9 (bottom row, middle panel); representative raw image of the NF case also shown in comparison at same instant in time (Fig. 9 bottom row, right panel)

floaters aggregate forming a single cluster (Lagarde et al. 2021). Such a condition was similarly visually observed in the current experiments (case NF); however, this happens on a much longer time scale and was outside our measurement time.

This relatively slow growth to a quasi-steady state in the NF case compared to the cases C1–C4 can be intuitively understood by identifying the most prominent physical mechanisms governing clustering in each case. In the NF case, capillary forces are the only mechanism driving the clustering, bringing floaters together through the "Cheerios effect" (Vella and Mahadevan 2005). In the latter, multiple clustering mechanisms are at play: the compressible nature of the free surface field brought about by the subsurface flow (in the form of positive and negative surface divergence), the presence of persistent vortices, and here too, capillary forces, typically acting at smaller spatial separations (capillary lengths). A consequence of the above is that the quasi-steady state in the flow cases is indicative of a balance between cluster formation and breakup, while in the NF case clusters continuously grow due to the absence of a physical mechanism leading to breakup. These differences in clustering mechanisms between flow and NF cases also lead to disparities in both the realizable size range of clusters as well as their spatial distribution (see Fig. 9). Cluster sizes in the NF case favor specific values, due to continuous merging of clusters of similar sizes, while in all the flow cases, a much more homogeneous distribution of cluster sizes is achievable due to continuous breakup and merging (see supplementary movies and discussion below). A more quantitative analysis, connecting the spatial and temporal scales of these different physical mechanisms and the floater clustering ones, is reserved for a future study, explicitly analyzing flow–floater interactions.

The temporal evolution of N_c discussed above (and shown in Fig. 10) includes the contribution of all floaters within clusters and does not differentiate between clusters of different sizes. To explore how different cluster sizes contribute to N_c over time (and for different turbulence levels), the temporal distribution of the *number of floaters* present in clusters of size S ($N(S)$) normalized by N is shown for cases C1–C4 and NF in Fig. 11 (left panel). Also shown is the *number of clusters* of size S ($n(S)$) normalized by the total number of clusters in the FOV (n_c) (Fig. 11 right panel). Warmer colors in the left and right panels represent a higher proportion of floaters within clusters of size S and of number of clusters of size S, respectively. For brevity, we focus here on the distribution of floaters within relatively small clusters ($S < 15$) due to their high frequency; however, larger clusters ($S > 100$) are also formed (see Fig. 12(a)) and are addressed later. Initially (at $t = 1$ sec), the majority of floaters is present in clusters of sizes $S = 2-3$ across all cases, as floaters begin clustering from an almost random distribution, as shown previously (see Fig. 9). Within $t = 10$ sec, the proportion of floaters present in smaller cluster sizes ($N(S < 5)$, see Fig. 11, left panel) decreases for C1–C4 while taking relatively longer for the NF case ($t \approx 30$ sec). This decrease of $N(S < 5)$ (see Fig. 11, left panel) is promoted by a redistribution of floaters or homogenization among different cluster sizes (from > 15 % to approximately between $2-5$ % of N) in cases C1 to C4. The time needed for this redistribution decreases with increasing turbulent activity (from C1 to C4, respectively). Despite the decreasing number of floaters in smaller-sized clusters ($N(S < 5)$, see Fig. 11, left panel), the latter still make up the majority of the total clusters formed at all times ($n(S < 5)$, see Fig. 11, right panel), which is consistently observed across flow cases (C1 to C4). In contrast, for the NF case, the percentage of smaller-sized clusters

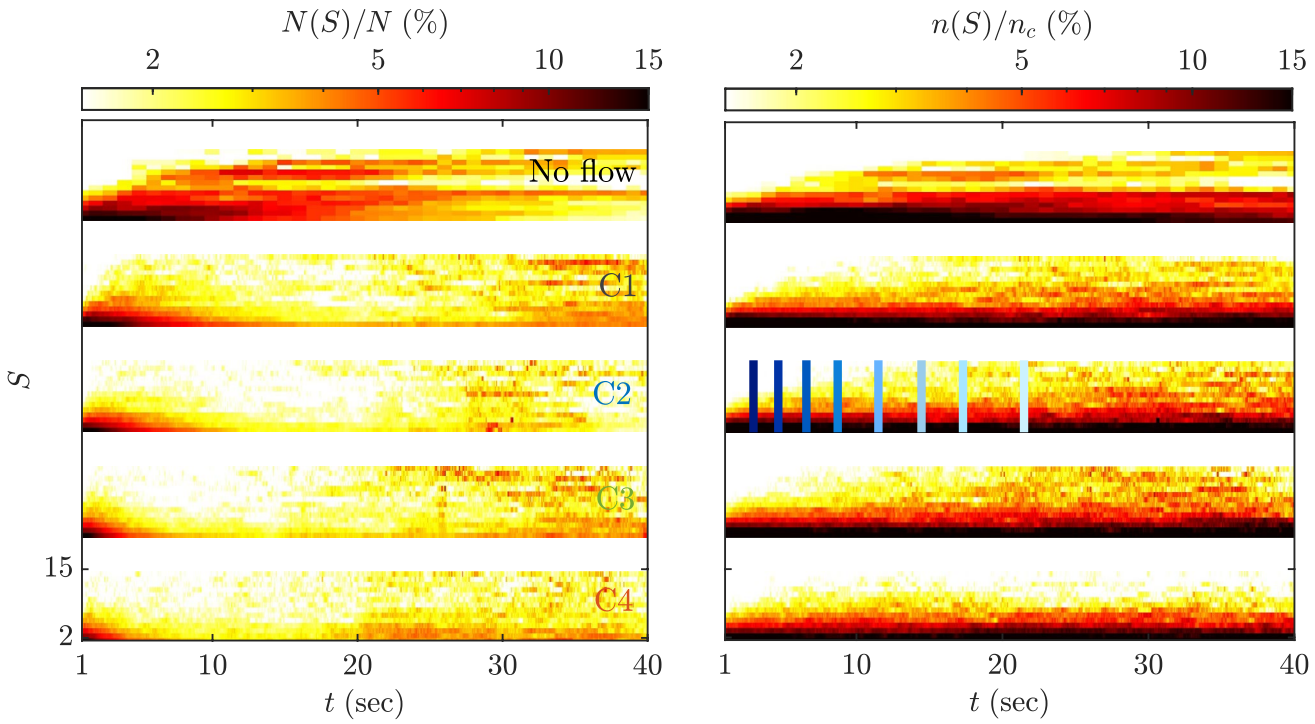

Fig. 11 Probability distribution of the number of floaters ($N(S)$) in clusters of size S (left) and of the number of clusters ($n(S)$) of size S (right), varying with time, for all different cases. Distributions are normalized by the total number of floaters (N) and clusters (n_c) in the FOV, respectively. Note that the colorbar is logarithmic. Solid vertical lines from darker to lighter shades of blue (in the direction of increasing time) in the right panel for case C2 indicate temporal slices of the distribution shown in Fig. 12(a)

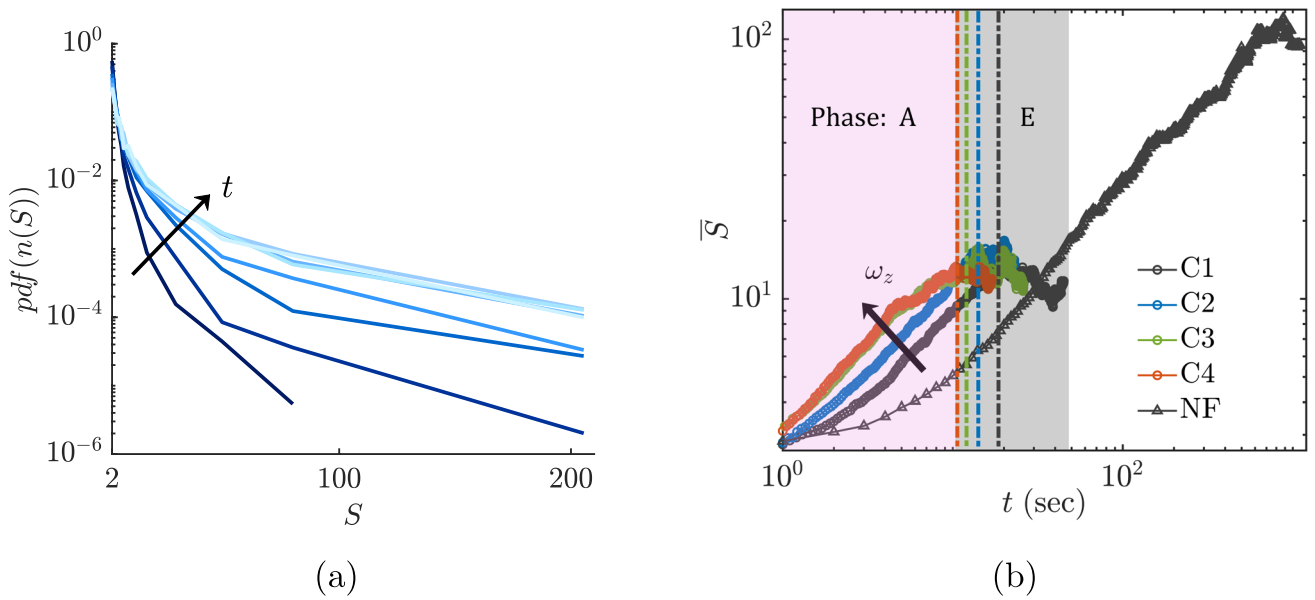

Fig. 12 (a) Pdf of the number of clusters ($n(S)$) as a function of cluster size S at different time instants. The latter correspond to temporal slices of the distribution of $n(S)/n_c$ at $t = [1.2, 2, 4.1, 6.3, 11.3, 14.8, 18.4, 26]$ sec, shown in the right panel of Fig. 11 for case C2 (darker to lighter shades of blue in the direction of increasing t, respectively). (b) Variation in the mean cluster size ($\overline{S}$) with time for different cases. Arrow shows increasing amplitude of ω_z from C1 to C4. Dash-dotted lines of corresponding colors indicate approximate time at which the equilibrium phase begins. The agglomeration (phase "A" in pink) and equilibrium (phase "E" in gray) phases are indicated for the flow cases (C1–C4)

eventually decreases at longer times as clusters continuously grow due to the absence of a breakup mechanism (see supplementary movie 2).

The relatively abundant smaller-sized clusters ($n(S < 5)$; see Fig. 11, right panel) are accompanied by a wide range of cluster sizes that are formed, including larger clusters. To explore how different cluster sizes formed contribute to the overall distribution of $n(S)$ (shown in Fig. 11, right panel), we examine temporal slices of this distribution for case C2 at different time instants t (see Fig. 12(a) in varying shades of blue). Note that similar trends were observed in the cases C1, C3, and C4 and are not shown here for brevity. As observed in Figure 11, initially (at $t = 1$ sec), cluster sizes of $S \lesssim 10$ dominate the distribution. With time, the tail of the pdf grows while the peak diminishes (see inset of Fig. 12(a)). The former reflects the formation of large clusters (for example, $S > 100$), while the latter indicates a reduction in floaters present in small clusters (for example, $S \lesssim 10$), which, however, remain more abundant. The pdfs collapse after $t \approx 11.3$ sec, indicating a quasi-steady state has been established between the number of smaller and larger clusters being formed and broken. This time scale closely matches to that observed in Fig. 10, where approximately 95 % of the floaters have clustered.

From a physical standpoint, size distributions in systems involving growth or fragmentation processes naturally arise in a lognormal form. Lognormal distributions are therefore widely used in literature to model, for example, the size distribution of particles, aerosols, airborne microbes (Limpert et al. 2001; Andersson 2021), and ice floes (Wadhams 1988), and have more recently been applied to predict the equilibrium aggregate size of cohesive particles formed in turbulence (Zhao et al. 2023). A lognormal distribution is thus a logical choice to model the cluster size distribution observed here, which fits this form closely and allows us to obtain the mean cluster size $\overline{S}$. The temporal variation of $\overline{S}$ is shown in Fig. 12(b) for all cases studied. For cases with flow, two distinct phases can be identified: an agglomeration phase (see Fig. 12(b) in pink) characterized by increasing $\overline{S}$ representing growing/merging clusters and an equilibrium phase/quasi-steady state (see Fig. 12(b) in gray) characterized by a plateau in $\overline{S}$ representing a balance between clusters forming and breaking. The "wiggles" around the plateau result from $\overline{S}$ being estimated from a reduced statistical sampling as fewer clusters remain in the FOV due to floaters leaving over time. The equilibrium phase appears to be reached by approximately $t \approx 10$ (C4)–18 sec (C1) (see dash-dotted lines of corresponding colors in Fig. 12(b)), closely matching the time scales observed in Fig. 10. The rate of increase of $\overline{S}$ is more rapid with increasing turbulent activity (from C1 to C4, respectively). Notably, the trends in cases C3 and C4 show a near collapse similar to that observed in the temporal variation of N_c/N (see Fig. 10). A similar collapse in the pdfs of the corresponding free surface divergence (see Fig. 7(b)) qualitatively indicates the role of $\nabla \cdot \mathbf{u}$ in the observed clustering rate. It is interesting to note that at equilibrium, all the cases with flow exhibit similar mean cluster sizes. This implies that within the range of turbulence levels studied, the distribution of floaters in different cluster sizes is statistically similar at equilibrium regardless of the turbulence intensity. However, these trends are in stark contrast to the NF case with respect to the growth rate of $\overline{S}$ and the mean cluster size achieved (see Fig. 12(b)). The former is relatively slower in the NF case compared to cases C1–C4. Furthermore, there is a continuous growth in $\overline{S}$ in the NF case, representative of a prolonged agglomeration phase until all floaters aggregate, the latter resulting from an absence of a breakup mechanism. However, this final equilibrium state is not captured within the current FOV and measurement time, and the observed plateau in $\overline{S}$ (see Fig. 12(b)) for the NF case results from floaters leaving the FOV.

In the presence of flow (C1–C4), floaters cluster as they probe a compressible field at the free surface, accumulating at sinks ($\nabla \cdot \mathbf{u} < 0$) and fleeing sources ($\nabla \cdot \mathbf{u} > 0$) (Cressman et al. 2004). However, while clustering is driven by the local surface divergence field, the time required for floaters to reach a quasi-steady clustering state is much longer ($\approx 4\mathcal{T}_L$) compared to the surface divergence time scales ($\approx 0.25\mathcal{T}_\mathcal{L}$). This finding is consistent with previous studies: Measuring cluster evolution times through their local correlation dimension, Larkin et al. (2010) reported $\approx 1\mathcal{T}_\mathcal{L}$ in experiments of surface flow above HIT, while Lovecchio et al. (2003) reported longer time scales ($\approx 5\mathcal{T}_\mathcal{L}$) in direct numerical simulations of an open-channel flow. Furthermore, Lagrangian autocorrelation of particle clusters in open-channel flow (Li et al. 2025) and in surface flow above HIT (Qi et al. 2025) reported clustering timescales of approximately $1\mathcal{T}_\mathcal{L}$. As discussed in section 3.1, vortical features at the free surface exhibit relatively long lifetimes ($\approx \mathcal{T}_\mathcal{L}$; see Fig. 8(c)), consistent with recent estimates by Qi et al. (2025) and with the behavior of surface-attached vortices reported in literature (Shen et al. 1999; Babiker et al. 2023; Aarnes et al. 2025). The latter have been hypothesized to trap floating particles during their lifetimes thereby imprinting their scales on the formation of clusters and its distribution spatially (Chor et al. 2018; Li et al. 2025). The relative contributions and interplay among mechanisms important at the free surface such as $\nabla \cdot \mathbf{u}$, ω_z, and capillarity, each typically acting on different spatial and temporal scales in driving floater clustering, however, remain open questions. Addressing these questions requires surface velocity field measurements coupled with floater tracking to capture cluster formation

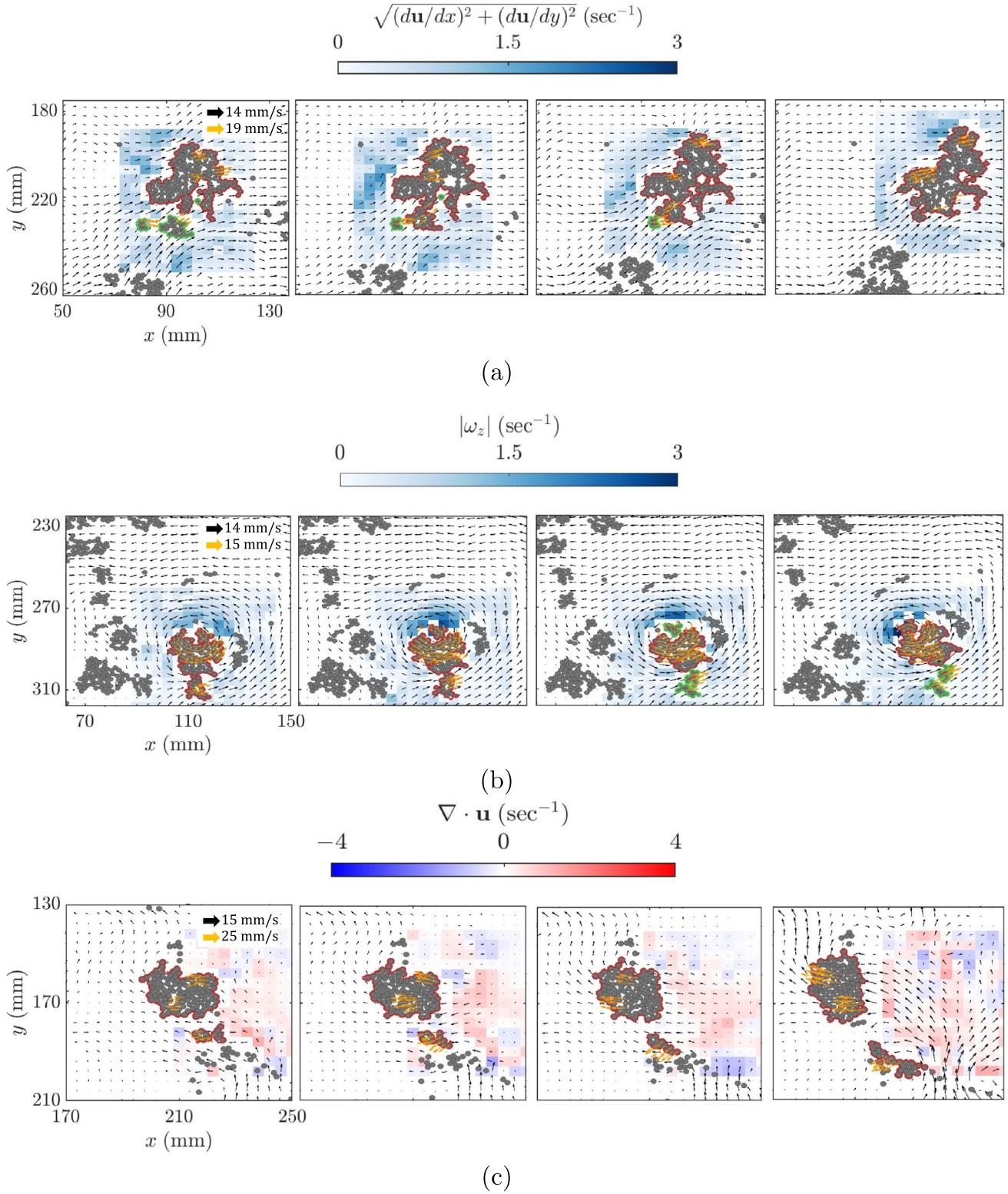

Fig. 13 Representative examples illustrating flow–floater interactions and their time evolution over ≈ 1 sec (left to right in time steps of ≈ 0.25 sec): (a) Clusters translating and merging under a flow velocity gradient. (b) Clusters rotating within a vortex. (c) Clusters subjected to a positive surface divergence event ($\nabla \cdot \mathbf{u} > 0$). Flow and floater velocity vectors are represented in black and orange, respectively. Note that not all floater velocities are shown for clarity

Table 3 Mean surface flow strength for all cases in the single-phase flow measurements and for two realizations of cases C1 and C4 shown in Fig. 14

Single phase	$\lvert\overline{u}\rvert/u_{rms}$	$\lvert\overline{v}\rvert/v_{rms}$	Two phase	$\lvert\overline{u}\rvert/u_{rms}$	$\lvert\overline{v}\rvert/v_{rms}$
C1	0.35	0.20	C1, R1	0.43	0.48
C2	0.15	0.24	C1, R2	0.32	0.30
C3	0.07	0.18	C4, R1	0.39	0.35
C4	0.19	0.12	C4, R2	0.18	0.19

and evolution. The proposed experimental technique provides access to both (see section 2.2), and preliminary results demonstrating its potential are presented next.

3.3 Flow–floater interactions

Representative examples of typical surface flow features interacting with floaters are shown in Fig. 13. These interactions, as seen through visual observations, represent more than 90 % of all the events (also see supplementary movie 1). When subject to a spatial gradient in flow velocity, clusters located in different regions of the gradient are advected at different velocities (see Fig. 13(a)). As a result of this velocity difference, the faster-moving cluster catches up to and merges with the slower one (see Fig. 13(a), where the clusters shown in green merge with the cluster in red). In addition to translation, clusters can rotate within surface-attached vortices (ω_z), the latter a common flow feature in free surface turbulence (see Fig. 13(b)). Spatial velocity gradients can result not only in the merging of clusters, as described above, but also in their breakup. Velocity gradients across the vortex and between the vortex and the surrounding flow can lead to cluster breakup (see Fig. 13(b), where clusters in green break away from the red cluster). That is, the shear imposed by the velocity gradient overcomes the attractive force between floaters, an aspect that can be quantified

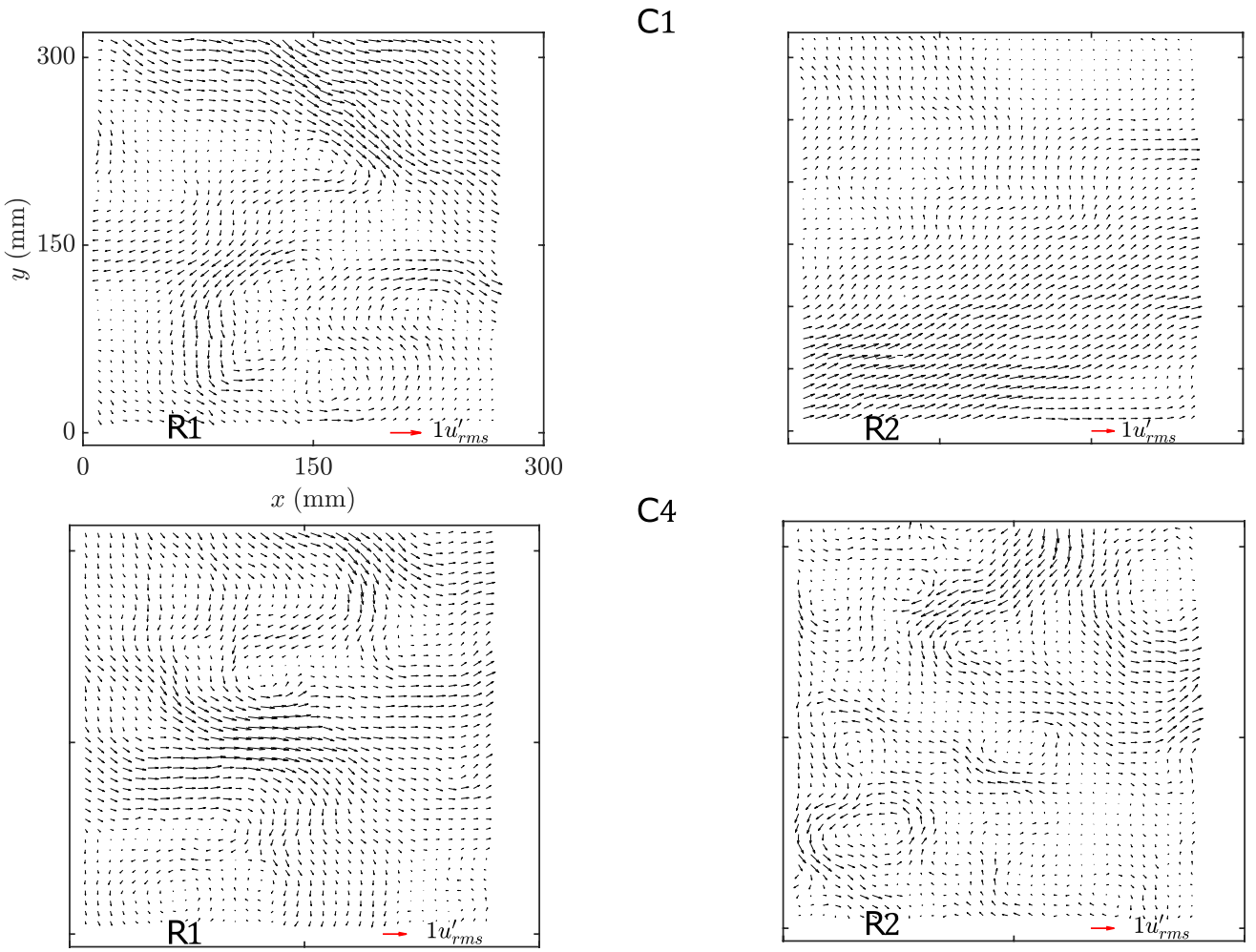

Fig. 14 Surface mean flow for two independent realizations (R1 and R2) of cases C1 and C4 (two phase, averaged over 2 min). Quantification of the mean flow strength is found in Table 3

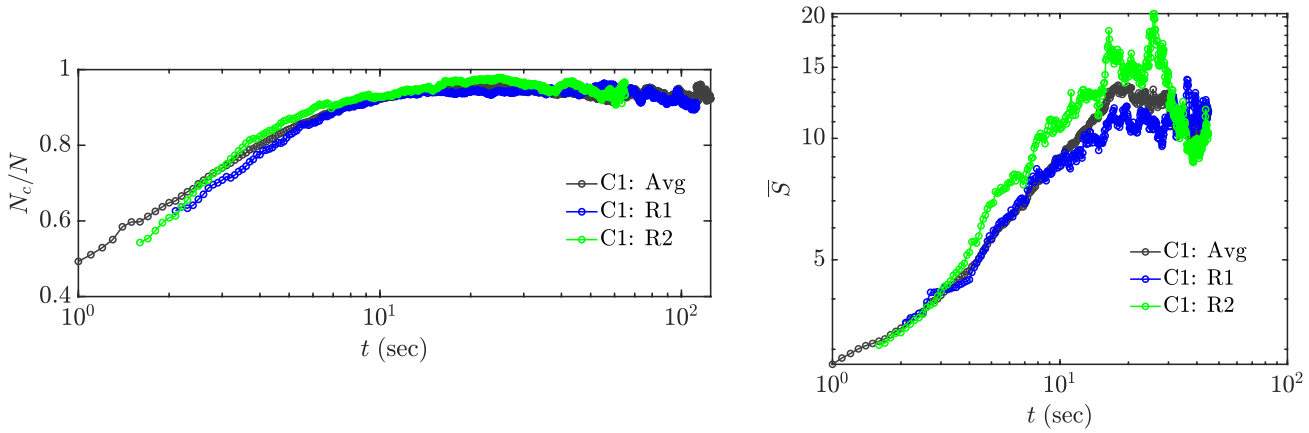

Fig. 15 Figs. 10 and 12(b) of the main manuscript, for case C1 (black, average over all realizations), re-plotted here with results from individual realizations R1 (green) and R2 (blue) (see Fig. 14 and Table 3)

using the proposed experimental technique. Moreover, the relatively long time scales of these vortices (see Fig. 8(c)) can play an important role in both spatial distribution of clusters and the overall floater dispersion.

Along with persistent vortices, the free surface is populated by positive ($\nabla \cdot \mathbf{u} > 0$) and negative ($\nabla \cdot \mathbf{u} < 0$) surface divergence events that have relatively shorter temporal durations (see Fig. 8(d)). A typical $\nabla \cdot \mathbf{u} > 0$ event is shown in Fig. 13(c) (characterized by outward pointing velocity vectors at the location of the source (in red); see second panel of the figure). Clusters in the vicinity of the positive surface divergence event are pushed away with floaters within clusters accelerating. In addition, the morphology of clusters appears to change as they move (for example, see cluster in red located between $y = 150$ mm and $y = 180$ mm). These examples illustrate a notable interplay between the floater behavior and different surface flow features. A detailed quantification of the flow–floater dynamics is inherently complex; however, the proposed relatively simple measurement setup already provides valuable insights into such dynamics. A more systematic analysis of these interactions is currently being pursued and will be the focus of future work.

4 Conclusions

We have presented an experimental method to study dispersed two-phase flows at an air–water interface. A relatively flat free surface laden with spherical floating particles ("floaters") above a low-mean nearly homogeneous turbulent flow is studied to demonstrate the applicability of this technique, the latter produced in a turbulence box actuated by a 10×10 synthetic jet array. Using a relatively simple setup of two LED panels and a single camera, we simultaneously measure the surface flow field using planar particle image velocimetry (PIV) and track floaters throughout the field of view. Specifically, we have employed the proposed technique to characterize the single-phase flow field and the clustering statistics of floaters for varying turbulence levels (the flow cases C1–C4), as well in the absence of a subsurface flow (the NF case). The former is achieved by changing the pump nozzle-to-free surface distance (h).

Following the identification and classification of floater clusters, we utilized them to analyze influence of turbulence levels on cluster size distributions and their evolution. We showed that through the temporal evolution of different cluster sizes, we can distinguish between capillary-driven clustering in the NF case from turbulence-driven clustering in the cases C1–C4. The former leads to the formation of specific cluster sizes while the latter to a more homogeneous distribution of cluster sizes (also see supplementary movies). Furthermore, the growth of clusters over time, which we quantify using the mean cluster size, is relatively slower in the NF case compared to cases C1–C4. The former exhibits a prolonged agglomeration phase (without cluster breakup) while the latter exhibits a relatively short agglomeration phase followed by an equilibrium phase characterized by a balance between clusters forming and breaking. In addition, increasing the turbulence level (cases C1 →C4) shortens the time required for clustering to reach the equilibrium phase. Nevertheless, the equilibrium phase is statistically similar in terms of the distribution of cluster sizes, regardless of the turbulence level.

To provide further insight into the temporal dynamics of the cluster size distributions presented here such as from an instantaneous perspective would require analysis

on cluster formation and evolution with specific flow features. This is an aspect that can be addressed by surface velocity field measurements coupled with floater tracking, something accessible by the current experimental technique. A detailed exploration of this, however, will be presented in a future study. We anticipate the applicability of this technique to enhance our understanding of floater-laden turbulent surfaces, a family of flows with notable environmental relevance.

Appendix: Mean surface flow

Here we quantify the time-averaged surface mean flow in our facility to assess any potential effects on clustering and facilitate comparisons with other similar RASJA configurations. Note that for the rms quantities used in the main manuscript, a different mean was subtracted (see equation 1 and the discussion in section 3.1).

As described in section 2 (see also Table 1), single-phase flow measurements were acquired over ≈ 2 hours. For the two-phase flow on the other hand, 10 independent, time-resolved runs were acquired, each lasting ≈ 2 min, limited by the time that the floaters remained within the field of view. The time-averaged surface flow fields of the two-phase flow for two independent realizations of cases C1 and C4 are shown in Fig. 14. Across all datasets, the direction/pattern of the resulting mean flow varies markedly, even between different realizations at the same turbulence level. That is, the mean surface flow pattern is neither consistently produced nor persistently present. The strength of these average fields (see Table 3) is comparable to those reported for similar single-planar RASJA setups with bulk subsurface measurements (for instance, Nezami and Johnson (2024): $\overline{u}/u_{rms} = 0.25$ and $\overline{v}/v_{rms} = 0.33$).

It is important to note that mean spatial gradients, specifically those associated with surface divergence ($\nabla \cdot \overline{\mathbf{u}}$), affect floater clustering over time scales that are significantly longer than those of turbulent fluctuations observed in Figs. 10 and 12(b). Thus, mean spatial gradients have a negligible effect on floater clustering, the latter which is of interest in this work. The negligible effect of mean spatial gradients on floater clustering can be further confirmed by the fact that, despite variations in both direction and magnitude of the mean surface flow (and its spatial gradients) among realizations at the same turbulence level in the two-phase cases (see Fig. 14), the temporal evolution of clustering and its associated time scales remain quantitatively the same (see Fig. 15).

Supplementary Information The online version contains supplementary material available at https://doi.org/10.1007/s00348-026-04185-3.

Acknowledgements The authors would like to gratefully acknowledge the help of the DEMO team (Martijn Karsten, Daniel van Baarle, Bart van der Lubbe), Bart Hoek, Jan Graafland, and Jasper Ruijgrok for their assistance in building the experimental facility. The authors would like to thank Edwin Overmars and Gertjan Mulders for their technical assistance during the experimental campaign.

Author contributions A.A. involved in investigation, conceptualization, methodology, visualization, validation, formal analysis, writing—original draft. C.P. took part in conceptualization, methodology, supervision, writing—review & editing. A.L. took part in conceptualization, methodology, supervision, writing—review & editing.

Funding This study is internally funded.

Data availability All data and codes will be made available upon request and are currently prepared to be uploaded on a data repository.

Declarations

Conflict of interest The authors report no conflict of interest.

References

Aarnes JR, Babiker OM, Xuan A, Shen L, Ellingsen SÅ (2025) Vortex structures under dimples and scars in turbulent free-surface flows. J Fluid Mech 1007(A38):1–32

Abraham ER (1998) The generation of plankton patchiness by turbulent stirring. Nature 391:577–580

Andersson A (2021) Mechanisms for log normal concentration distributions in the environment. Sci Rep 11(16418):1–7

Babiker OM, Bjerkebæk I, Xuan A, Shen L, Ellingsen SÅ (2023) Vortex imprints on a free surface as proxy for surface divergence. J Fluid Mech 964(R2):1–13

Baker L, Frankel A, Mani A, Coletti F (2017) Coherent clusters of inertial particles in homogeneous turbulence. J Fluid Mech 833:364–398

Banerjee S (1994) Upwellings, downdrafts, and whirlpools: Dominant structures in free surface turbulence. Appl Mech Rev 47(6):166–172

Bang JY, Pujara N (2023) Homogeneous turbulence in a random-jet-stirred tank. Exp Fluids 64(185):1–22

Brocchini M, Peregrine DH (2001) The dynamics of strong turbulence at free surfaces. Part 1. Descript J Fluid Mech 449:225–254

Brumley BH, Jirka GH (1987) Near-surface turbulence in a grid-stirred tank. J Fluid Mech 183:235–263

Bullee PA, Weichert S, Nore A, Li L, Ellingsen SÅ, Hearst RJ (2024) The influence of water turbulence on surface deformations and

the gas transfer rate across an air-water interface. Exp Fluids 65(132):1–15
Carter D, Petersen A, Amili O, Coletti F (2016) Generating and controlling homogeneous air turublence using random jet arrays. Exp Fluids 57(189):1–15
Chamecki M, Chor T, Yang D, Meneveau C (2019) Material transport in the ocean mixed layer: recent developments enabled by large eddy simulations. Rev Geophys 57:1338–1371
Chen B, Yang D, Meneveau C, Chamecki M (2016) Effects of swell on transport and dispersion of oil plumes within the ocean mixed layer. J Geophys Res Oceans 121:3564–3578
Chor T, Yang D, Meneveau C, Chamecki M (2018) Preferential concentration of noninertial buoyant particles in the ocean mixed layer under free convection. Phys Rev Fluids 3(064501):1–18
Cressman JR, Davoudi J, Goldburg WI, Schumacher J (2004) Eulerian and Lagrangian studies in surface flow turbulence. New J Phys 6(53):1–25
Douady S, Couder Y, Brachet ME (1991) Direct observation of the intermittency of intense vorticity filaments in turbulence. Phys Rev Lett 67:983–986
Eckhardt B, Schumacher J (2001) Turbulence and passive scalar transport in a free-slip surface. Phys Rev E 64(016314):1–10
Ference J-S, Néda Z (2007) On the size distribution of poisson voronoi cells. Physica AStat Mech Applics 385(2):518–526
Goldburg WI, Cressman JR, Vörös Z, Eckhardt B, Schumacher J (2001) Turbulence in a free surface. Phys Rev E 63(065303):1–4
Guo X, Shen L (2010) Interaction of a deformable free surface th statistically steady homogeneous turbulence. J Fluid Mech 658:33–62
Hassan YA, Canaan RE (1991) Full-field bubbly flow velocity measurements using a multiframe particle tracking technique. Exp Fluids 12:49–60
Herlina H, Wissink JG (2019) Simulation of air-water interfacial mass transfer driven by high-intensity isotropic turbulence. J Fluid Mech 860:419–440
Hopfinger EJ, Toly J-A (1976) Spatially decaying turbulence and its relation to mixing across density interfaces. J Fluid Mech 78:155–175
Hwang W, Eaton JK (2004) Creating homogeneous and isotropic turbulence without a mean flow. Exp Fluids 36:444–454
Johnson BA, Cowen EA (2018) Turbulent boundary layers absent mean shear. J Fluid Mech 835:217–251
Jong J, Cao L, Woodward SH, Salazar JPLC, Collins LR, Meng H (2009) Dissipation rate estimation from PIV in zero-mean isotropic turbulence. Exp Fluids 46:499–515
Komori S, Ueda H, Ogino F, Tokuro M (1982) Turbulent structure and transport mechanism at the free surface in an open channel flow. Int J Heat Mass Transfer 25(4):513–521
Kumar S, Gupta R, Banerjee S (1998) An experimental investigation of the characteristics of free-surface turbulence in channel flow. Phys Fluids 10(2):437–456
Lagarde A, Josserand C, Protière S (2021) Transient aggregation of particles at interfaces. Phys Rev Fluids 6(084307):1–11
Larkin J, Goldburg WI (2010) Decorrelating a compressible turbulent flow: An experiment. Phys Rev E 82(016301):1–6
Larkin J, Goldburg WI, Bandi MM (2010) Time evolution of a fractal distribution: Particle concentrations in free-surface turbulence. Physica D 239:1264–1268
Li Y, Meneveau C (2005) Origin of non-gaussian statistics in hydrodynamic turbulence. Phys Rev Lett 95(164502):1–4
Li Y, Sanness Salmon H, Hassaini R, Chang K, Mucignat C, Coletti F (2025) Spatiotemporal scales of motion and particle clustering in free-surface turbulence. Phys Rev Fluids 10(034602):1–19
Limpert E, Stahel WA, Abbt M (2001) Log-normal distributions across the sciences: Keys and clues. Bioscience 51:341–352
Lovecchio S, Marchioli C, Soldati A (2003) Time persistence of floating-particle clusters in free-surface turbulence. Phys Rev E 88(033003):1–6
Maalouly M, Lapeyre G, Cozian B, Mompean G, Berti S (2023) Particle dispersion and clustering in surface ocean turbulence with ageostrophic dynamics. Phys Fuids 35:126601
Malik NA, T, D., A., P.D.: Particle tracking velocimetry in three dimensional flow. Experiments in Fluids 15, 279–294 (1993)
McKenna SP, McGillis WR (2004) The role of free-surface turbulence and surfactants in air-water gas transfer. Int J Heat Mass Transf 47:539–553
Meacham J, Berloff P (2023) On clustering of floating tracers in random velocity fields. J Adv Model Earth Syst 15:1–18
Monchaux R, Bourgoin M, Cartellier A (2010) Preferential concentration of heavy particles: A Voronon$\ddot{i}$ analysis. Physics of Fuids 22(10):103304
Mouri H, Takaoka H, Hori A, Kawashima Y (2002) Probability density function of turbulence velocity fluctuations. Physical Review E 65(5): 056304, 1–7
Muraro F, Dolcetti G, Nichols A, Tait SJ, Horoshenkov KV (2021) Free-surface behaviiour of shallow turbulent flows. J Hydraul Res 59:1–20
Nagaosa R (1999) Direct numerical simulation of vortex structures and turbulent scalar transfer across a free surface in a fully developed turbulence. Phys Fluids 11(6):1581–1595
Nezami AG, Johnson BA (2024) Evolution of turbulence using a random jet array. Phys Rev Fluids 9(074610):1–23
Nieuwstadt FTM, Boersma BJ, Westerweel J (2015) Turbulence: Introduction to Theory and Applications of Turbulent Flows. Springer, Delft, The Netherlands
Nishino K, Kasagi N, Hirata M (1989) Three-dimensional particle tracking velocimetry based on automated digital image processing. J Fluids Eng 111:384–391
Oulette NT, Xu H, Bodenschatz E (2006) A quantitative study of three-dimensional langrangian particle tracking algorithms. Exp Fluids 40:301–313
Pan Y, Banerjee S (1995) A numerical study of free-surface turbulence in channel flow. Phys Fluids 7(7):1649–1664
Pérez-Alvarado A, Mydlarski L, Gaskin S (2016) Effect of the driving algorithm on the turbulence generated by a random jet array. Exp Fluids 57(20):1–15
Perot B, Moin P (1995) Shear-free turbulent boundary layers. part 1. physical insights into near-wall turbulence. Journal of Fluid Mechanics 295, 199–227
Petersen AJ, Baker L, Coletti F (2019) Experimental study of inertial particles clustering and settling in homogeneous turbulence. J Fluid Mech 864:925–970
Protière S (2023) Particle rafts and armored droplets. Annu Rev Fluid Mech 55(1):459–480
Qi Y, Li Y, Coletti F (2025) Small-scale dynamics and structure of free-surface turbulence. J Fluid Mech 1007(A3):1–27
Rashidi M (1997) Burst-interface interactions in free surface turbulent flows. Phys Fluids 9(11):3485–3501
Ruth DJ, Coletti F (2024) Structure and energy transfer in homogeneous turbulence below a free surface. J Fluid Mech 1001(A46):1–31
Sanness Salmon HR, Baker LJ, Kozarek JL, Coletti F (2023) Effect of Shape and Size on the Transport of Floating Particles on the Free Surface in a Natural Stream. Water Resour Res 59:1–22
Savelsberg R, van de Water W (2009) Experiments on free-surface turbulence. J Fluid Mech 619:95–125
Sebille E, Aliani S, Law KL, Maximenko N, Alsina JM, Bagaev A, Bbergmann M, Chapron B, Chubarenko I, Cózar A, Delandmeter P, Egger M, Fox-Kemper B, Garaba SP, Goddijn-Murphy L, Hardesty BD, Hoffman MJ, Isobe A, Jongedijk CE, Kaandorp MLA, Khatmullina L, Koelmans AA, Kukulka T, Laufkötter C,

Lebreton L, Lobelle D, Maes C, Martinez-Vicente V, Maqueda MAM, Poulain-Zarcos M, Rodríguez E, Ryan PG, Shanks AL, Shim WJ, Suaria G, Thiel M, Bremer TS, Wichmann D (2020) The physical oceanography of the transport of floating marine debris. Environ Res Lett 15(023003):1–32

Shen L, Zhang X, Yue DKP, Triantafyllou GS (1999) The surface layer for free surface turbulent flows. J Fluid Mech 386:167–212

Sumbekova S, Cartellier A, Aliseda A, Bourgoin M (2017) Preferential concentration of inertial sub-Kolmogorov particles: The roles of mass loading of particles, Stokes numbers, and Reynolds numbers. Phys Rev Fluids 2:024302

Sutherland BR, DiBenedetto M, Kaminski A, van den Bremer T (2023) Fluid dynamics challenges in predicting plastic pollution transport in the ocean: A perspective. Phys Rev Fluids 8(070701):1–20

Tagawa Y, Mercado JM, Prakash VN, Calzavarini E, Sun C, Lohse D (2012) Three-simensional Lagrangian Voronoi$\ddot{i}$ analysis for clustering of particles and bubbles in turbulence. J Fluid Mech 693:201–215

Thompson SM, Turner JS (1975) Mixing across an interface due to turbulence generated by an oscillating grid. J Fluid Mech 67:349–368

Tokgoz S, Elsinga GE, Delfos R, Westerweel J (2012) Spatial resolution and dissipation rate estimation in taylor–couette flow for tomographic PIV. Exp Fluids 53:561–583

Variano EA, Cowen EA (2008) A random-jet-stirrred turbulence tank. J Fluid Mech 604:1–32

Variano EA, Cowen EA (2013) Turbulent transport of a high-Schmidt-number scalar near an air-water interface. J Fluid Mech 731:259–287

Vella D, Mahadevan L (2005) The "Cheerios effect''. Am J Phys 73:817–825

Voth GA, Porta A, Crawford AM, J, A, E, B.: Measurement of particle accelerations in fully developed turbulence. Journal of Fluid Mechanics 469, 121–160 (2002)

Voth GA, Satyanarayan K, Bodenschatz E (1998) Lagrangian acceleration measurements at large Reynolds numbers. Physics of Fuids 10:2268–2280

Wadhams P (1988) Winter Observations of Iceberg Frequencies and Sizes in the South Atlantic Ocean. J Geophys Res 93(C4):3583–3590

Walker DT, Leighton RI, Garza-Rios LO (1996) Shear-free turbulence near a flat free surface. J Fluid Mech 320:19–51

Westerweel J, Scarano F (2005) Universal outlier detection for PIV data. Exp Fluids 39(6):1096–1100

Zhao K, Vowinckel B, Hsu T-J, Bai B, Meiburg E (2023) Cohesive sediment: intermediate shear produces maximum aggregate size. J Fluid Mech 965(A5):1–17